The Meteoritical Society

Meteoritics & Planetary Science 54, Nr 6, 1262–1282 (2019)
doi: 10.1111/maps.13278

Shock-induced microtextures in lunar apatite and merrillite

Ana ČERNOK[1,6,*], Lee Francis WHITE[2,3], James DARLING[4], Joseph DUNLOP[4], and Mahesh ANAND[1,5]

[1]School of Physical Sciences, The Open University, Walton Hall, Milton Keynes MK7 6AA, UK
[2]Centre for Applied Planetary Mineralogy, Department of Natural History, Royal Ontario Museum, Toronto, ON M5S 2C6, Canada
[3]Department of Earth Sciences, University of Toronto, Toronto, ON M5S 3B1, Canada
[4]School of Earth & Environmental Sciences, University of Portsmouth, Burnaby Road, Portsmouth PO1 3QL, UK
[5]Department of Earth Sciences, The Natural History Museum, London SW7 5BD, UK
[6] Current address: Planetary Mineralogy, Royal Ontario Museum, 100 Queens Park, Toronto, ON, Canada
*Corresponding author. E-mail: acernok@rom.on.ca

(Received 11 September 2018; revision accepted 12 February 2019)

Abstract–Apatite and merrillite are the most common phosphate minerals in a wide range of planetary materials and are key accessory phases for in situ age dating, as well as for determination of the volatile abundances and their isotopic composition. Although most lunar and meteoritic samples show at least some evidence of impact metamorphism, relatively little is known about how these two phosphates respond to shock-loading. In this work, we analyzed a set of well-studied lunar highlands samples (Apollo 17 Mg-suite rocks 76535, 76335, 72255, 78235, and 78236), in order of displaying increasing shock deformation stages from S1 to S6. We determined the stage of shock deformation of the rock based on existing plagioclase shock-pressure barometry using optical microscopy, Raman spectroscopy, and SEM-based panchromatic cathodoluminescence (CL) imaging of plagioclase. We then inspected the microtexture of apatite and merrillite through an integrated study of Raman spectroscopy, SEM-CL imaging, and electron backscatter diffraction (EBSD). EBSD analyses revealed that microtextures in apatite and merrillite become progressively more complex and deformed with increasing levels of shock-loading. An early shock-stage fragmentation at S1 and S2 is followed by subgrain formation from S2 onward, showing consistent decrease in subgrain size with increasing level of deformation (up to S5) and finally granularization of grains caused by recrystallization (S6). Starting with 2°–3° of intragrain crystal-plastic deformation in both phosphates at the lowest shock stage, apatite undergoes up to 25° and merrillite up to 30° of crystal-plastic deformation at the highest stage of shock deformation (S5). Merrillite displays lower shock impedance than apatite; hence, it is more deformed at the same level of shock-loading. We suggest that the microtexture of apatite and merrillite visualized by EBSD can be used to evaluate stages of shock deformation and should be taken into account when interpreting in situ geochemically relevant analyses of the phosphates, e.g., age or volatile content, as it has been shown in other accessory minerals that differently shocked domains can yield significantly different ages.

INTRODUCTION

Apatite $Ca_5(PO_4)_3(F, Cl, OH)$ is a mineral belonging to the phosphate group, crystallizing in hexagonal 6/m symmetry (Hughes and Rakovan 2002; Hughes 2015). In lunar samples, apatite is found among all major lithologies, except in anorthosites (Heiken et al. 1991), both in Apollo collections and lunar meteorites. Composition of apatite from mare basalts is close to pure fluorapatite (e.g., Jolliff et al.

1993) with minor amounts of OH and Cl, whereas apatite in highlands samples can contain significantly more Cl (e.g., Barnes et al. 2014). Merrillite is a nominally anhydrous phosphate mineral with an ideal composition of $Ca_9Na(Fe,Mg)(PO_4)_7$ crystallizing in trigonal R3c symmetry (Hughes et al. 2006; Xie et al. 2015), but it has been found to contain a small amount of volatile species in some meteorites (e.g., McCubbin et al. 2014). In lunar rocks, merrillite is found to accommodate significant amounts of REEs in its structure, resulting in a very complex stoichiometric formula (Hughes et al. 2006; Jolliff et al. 2006). Merrillite is an anhydrous endmember of the merrillite–whitlockite solid-solution series, and whitlockite is described as its hydrous isostructural counterpart (Hughes et al. 2008). Due to this structural similarity, merrillite was misinterpreted as lunar whitlockite for several decades (Jolliff et al. 2006; Jolliff 2014). Merrillite can form by dehydrogenation of whitlockite (Hughes et al. 2008) and it has recently been shown that this transformation can be shock-induced (Adcock et al. 2017). The high-pressure polymorph formed at an even higher compression regime is tuite (Xie et al. 2002, 2003), which can also form by compression of apatite (Xie et al. 2013).

Apatite and merrillite are the most common phosphate minerals in a wide range of planetary materials (Heiken et al. 1991; Jones et al. 2014, 2016; Hughes 2015; McCubbin and Jones 2015) that are often found in textural association with each other. They are the main host of phosphorous, REEs, and volatiles (F, Cl, OH) in lunar and meteoritic samples (Jolliff et al. 1993; McCubbin et al. 2014). As common accessory minerals in lunar rocks and other planetary materials, apatite and merrillite are being increasingly exploited to gain insight into key planetary processes. For example, these accessory minerals are often analyzed to obtain the absolute ages of planetary materials, and the number of studies employing routine protocols for Pb-Pb and U-Pb age determinations of phosphates has been growing over the past two decades (e.g., Göpel et al. 1994; Terada et al. 2005, 2007; Merle et al. 2014; Chew and Spikings 2015; Snape et al. 2016; Thiessen et al. 2017). Recent technical advancements in secondary ion mass spectrometry have further facilitated in situ studies of abundances and isotopic composition of volatiles (mainly in apatite) and in situ age dating of phosphates (Terada et al. 2005, 2007; Merle et al. 2014; Snape et al. 2016; Thiessen et al. 2017). After discovery of water in lunar volcanic glasses (Saal et al. 2008), apatite became the target mineral for investigating the origin and history of volatiles in the lunar interior (Boyce et al. 2010, 2014; McCubbin et al. 2010, 2015; Greenwood et al. 2011; Tartèse and Anand 2013; Tartèse et al. 2013, 2014; Anand 2014; Anand et al. 2014; Barnes et al. 2014, 2016). Lunar apatite is preferred for volatile studies over merrillite because the latter is essentially anhydrous in lunar samples (Jolliff et al. 2006). Likewise, apatite and merrillite became a common target for studying volatiles in the meteoritic record, including Martian meteorites (McCubbin et al. 2014; Bellucci et al. 2017) and meteorites thought to have originated from Vesta (Sarafian et al. 2013; Barrett et al. 2016). Recently, apatite has also been recognized as a potential oxybarometer (Economos et al. 2017; Konecke et al. 2017). In terrestrial samples, apatite is considered a versatile mineral to provide insights into various geological characteristics and processes, ranging from magmatic (Webster and Piccoli 2015) to metasomatic processes (Harlov 2015), to geochronology (Chew and Spikings 2015) to understanding the magma source regions based on apatite trace element compositions (Mao et al. 2016; Bruand et al. 2017). Although the anhydrous whitlockite has been previously reported in rocks from Siberia (Ionov et al. 2006), mineral merrillite is not generally reported in terrestrial samples. In terrestrial samples, hydrous whitlockite is common, but merrillite occurs only as a minor solid solution with whitlockite (Hughes et al. 2008).

Although most lunar and meteoritic samples show at least some evidence of impact metamorphism, relatively little is known about how microtexture of apatite and merrillite develops in response to shock loading. Terrestrial apatite from several different impact structures is observed to display planar microstructures (Cavosie and Centeno 2014; McGregor et al. 2018) or granular, recrystallization features (Alwmark et al. 2017; Kenny et al. 2019b). In addition to naturally shocked grains, experimentally shocked apatite has also been shown to display planar microstructures (Sclar and Morzenti 1972). Our study was designed to understand microstructural deformation of apatite and merrillite in response to variable shock loading. It is assessed based on deformation observed in coexisting plagioclase, a well-established shock barometer in planetary materials (e.g., Stöffler et al. 1991; Rubin et al. 1997; Fritz et al. 2017).

The Shock-Pressure Barometry

To estimate the extent of shock-induced deformation experienced by a host rock, various shock barometers are used. However, the application of the most refined shock barometer—quartz (e.g., Stöffler and Langenhorst 1994)—is limited to terrestrial and more felsic rocks that are scarce in lunar and meteoritic samples. Therefore, different shock barometers were employed to study quartz-free planetary materials,

relying on other major minerals, e.g., feldspar solid-solution series, and in particular plagioclase (Stöffler et al. 1991; Rubin et al. 1997; Johnson et al. 2002; Johnson 2012; Jaret et al. 2014; Pickersgill et al. 2015; Fritz et al. 2017; Pernet-Fisher et al. 2017). At the highest observed shock deformation, for example, in Martian and other meteorites, assemblages of high-pressure mineral polymorphs are used to estimate peak-shock conditions (e.g., in Tissint, Baziotis et al. 2013; Walton et al. 2014). Although the feldspar solid-solution series has been recognized as a useful proxy for shock deformation, due to the lack of experimental data at pressures below ~10 GPa, there is only a rough classification for feldspar deformation at lower pressures, with the higher pressure end, above plagioclase isotropization (>20 GPa), being substantially more refined (e.g., Fritz et al. 2005). Several recent studies have targeted natural samples in the need to better constrain the lower end of the shock scale for quartz-free samples, and feldspar and plagioclase series were proven to be an excellent proxy (Jaret et al. 2014; Pickersgill et al. 2015). This is of particular importance for studies of the early lunar crust, because the shock state of the lunar anorthosites is estimated to be on average <15 GPa, with only rare presence of highland rocks exposed to shock pressures exceeding 30 GPa (Pernet-Fisher et al. 2017). This implies that most of the plagioclase was exposed to shock pressures insufficient to cause solid-state transformation to plagioclase diaplectic glass (>20–24 GPa for anorthitic composition).

Microstructural studies of accessory minerals that are used as reliable geochronometers—zircon, baddeleyite, xenotime, or monazite—have provided an entirely new approach to assess shock deformation at μm scale (e.g., Moser et al. 2013; Erickson et al. 2015; Darling et al. 2016; White et al. 2017). In particular, xenotime and baddeleyite were observed to have undergone significant deformation at lower shock pressures (Cavosie et al. 2016; White et al. 2018a, 2018b). Importantly, these studies highlighted the importance of understanding the microstructure of targeted geochronometers when interpreting their complex U-Pb and Pb-Pb ages. Due to their grain size that is often smaller than ~100 μm, accessory minerals cannot be inspected by conventional techniques used to assess the shock state of major minerals, such as optical microscopy or even in-house X-ray diffraction (μ-XRD) (Pickersgill et al. 2015). Hence, their microtexture is best inspected by electron backscatter diffraction (EBSD)—a nondestructive, time- and cost-efficient technique. Similar to secondary electron- (SE) and backscatter electron (BSE) microscopy, an electron beam is rastered across an entire grain to create an image. However, in addition to surface and compositional imaging, EBSD can retrieve crucial textural information stored at sub-μm scale that is not affected by surface effects or chemical composition, and is therefore omitted by SE and BSE imaging (e.g., White et al. 2017).

For the purpose of this work, we chose a set of well-studied lunar highland samples collected by the Apollo 17 mission, most of which have not been previously assigned a shock level (see below). Optical, SE, and BSE microscopy of plagioclase, as well as the EBSD microstructural analysis of apatite and merrillite, were complemented with Raman spectroscopy and cathodoluminescence (CL) imaging. The stage of shock deformation of samples was established based on existing plagioclase shock-pressure barometry (Stöffler et al. 1991; Rubin et al. 1997; Jaret et al. 2014; Fritz et al. 2017). The results demonstrate an easy-to-quantify deformation scale sequence of lunar apatite and merrillite that can be of particular use when dealing with low-shock deformation. The type of work presented here has a great potential to aid in interpretation of complex in situ geochemical studies of apatite and merrillite, such as volatiles' budget, crystallization age, or timing of impact resetting.

SELECTION OF SAMPLES

While about one-third of lunar basaltic meteorites contain plagioclase diaplectic glass (Rubin 2015), it is generally rare among Apollo samples. Therefore, the Apollo rocks might seem unqualified for shock investigation of minerals. However, a significant advantage of the Apollo samples is that they have not been exposed to terrestrial weathering, to which phosphate minerals could be very sensitive (Flicoteaux and Lucas 1984). Five different lunar samples of Mg-suite norite and troctolite were selected for this study from the Apollo 17 collection, based on the increasing level of shock deformation: troctolite 76535, anorthositic troctolite 76335, *Civet Cat* norite fragment from the 72255 impact-melt breccia, and heavily shocked norites 78235 and 78236. All studied samples represent coherent rock specimens rather than polymict impact breccias, thus, avoiding complex shock histories and limiting the heterogeneity of shock distribution among fragments. At the same time, all of the selected samples above were previously characterized as compositionally pristine according to classification scheme of Warren (1993), meaning that they survived the meteoritic bombardment with sufficiently limited brecciation and melting such that their bulk compositions and in particular highly siderophile elements content are representative of individual, unmixed, endogenously igneous rocks.

The unshocked troctolite 76535 is one of the best studied samples within the Apollo collection, commonly referred to as "the least shocked rock from the Moon." It resembles an equilibrium cumulate texture of olivine, plagioclase, and clinopyroxene represented by smooth grain boundaries and 120° triple junctions. Abundant accessory minerals—apatite, merrillite, and baddeleyite—show the KREEP (K-potassium, REE—rare earth elements, P—phosphorous) affinity of this rock. Plagioclase is highly anorthitic (An_{96}). It is a coarse-grained plutonic rock, with evidence of extensive annealing and re-equilibration indicative of the rock emplacement at shallower depth (e.g., Dymek et al. 1975; Warren 1993). U-Pb ages suggest crystallization took place 4236 ± 15 Myr ago (Ma; Premo and Tatsumoto 1992). More recent geochronological studies report concordant Rb-Sr (4279 ± 52 Ma), ^{147}Sm-^{143}Nd (4307 ± 11 Ma), and ^{146}Sm-^{142}Nd (4299 + 29/−35 Ma) according to Borg et al. (2017) and older Pb-Pb ages (4375 ± 1 Ma) (Borg et al. 2013). Detailed discussion on the ages of Mg-suite rocks is given in Carlson et al. (2014).

The cataclastic troctolite 76335 is petrogenetically related to troctolite 76535. The rock is comprised of plagioclase (An_{96}) and orthopyroxene, with abundant accessory minerals (apatite, merrilite, chromite, baddeleyite, keiivite-Y, etc.) (Edmunson et al. 2010). It is heavily fractured, containing large undeformed mineral clasts, surrounded by very fine-grained monomineralic matrix, but no occurrence of impact melt has been reported. It is not a polymict impact breccia, as the original magmatic textures can still be recognized in the section. A shock stage has not been assigned to this sample. The rock has been dated as 4278 ± 6 Ma as defined by Sm-Nd isotopic system, but it shows significant disturbance in Rb-Sr systematics (Edmunson et al. 2007). A detailed summary on geochronology of this sample is provided in Carlson et al. (2014).

Civet Cat norite is a 2 cm clast within 72255 aphanitic impact-melt breccia (Stoeser et al. 1974). The fragment contains equal amount of plagioclase and orthopyroxene (Bersch et al. 1991). The rock shows evidence of severe shock deformation, in the form of kink-bands in pyroxene and formation of plagioclase diaplectic glass. However, the composition of the rock is preserved as pristine (Warren 1993). The age of this fragment is estimated at 3990 ± 30 Ma by Ar-Ar technique (Leich et al. 1975), and 4080 ± 50 Ma by Rb-Sr (Compston et al. 1975). No shock stage has been previously ascribed to the rock.

The heavily shocked norites 78235 and 78236 are extensively studied samples (e.g., Steele 1975; Hinthorne et al. 1977; Edmunson et al. [2009] and references therein). They appear to be an igneous orthopyroxene–plagioclase cumulate with little intercumulus accessory minerals and minor clinopyroxene (Winzer 1975), covered by a brown glass coating and intruded by glass veins derived by the shock melting of the whole rock (Jackson et al. 1975; Sclar and Bauer 1975; El Goresy et al. 1976). The composition of this brown glass corresponds to 50% orthopyroxene and 50% plagioclase of the whole norite. The extent of shock deformation has been assessed since the earliest studies (Sclar and Bauer 1975, 1976; El Goresy et al. 1976), with the peak shock pressure estimated to be in excess of 50 GPa. The orthopyroxene is heavily brecciated and displays mosaicism, undulatory extinction, and shock lamellae. The plagioclase shows different stages of shock metamorphism, indicative of inhomogeneous distribution of shock pressures and postshock temperatures. These range from mostly crystalline, birefringent cores, which grade into diaplectic glass and further toward the grain boundaries against pyroxene into rim of melted plagioclase glass. Crystalline plagioclase, diaplectic plagioclase glass, and plagioclase melted glass have identical compositions ($An_{93\text{-}96}$), but different refractive indices. This rock with strong KREEP signature contains abundant accessory minerals, including apatite, merrilite, Nb-rutile, baddeleyite, and zircon (Edmunson et al. 2009). A recent study found that the crystallization age of the shocked norite based on Pb-Pb systematics is 4333 ± 59 Ma, and it is concordant with Sm-Nd age of 4334 ± 37 Ma (Edmunson et al. 2009). However, the same study found significant disturbance in Rb-Sr isochron that is explained by the heavy shock history of the rock. Interestingly, the Ar-Ar age of 4188 ± 13 Ma (Fernandes et al. 2013) does not show any disturbance of the Ar-Ar systematics at an earlier date. The shocked norite was subjected to numerous geochronological studies in the past and a detailed summary is given in Carlson et al. (2014).

ANALYTICAL TECHNIQUES

Polished thin sections of all Apollo samples studied in this work were prepared at NASA Johnson Space Center in a water-free medium, and mounted onto a glass slide using araldite epoxy (see Tartèse et al. [2013] for further details).

Secondary Electron Microscopy and Panchromatic Cathodoluminescence Imaging

The polished thin sections were carbon coated and examined using a Quanta 3-D focused ion beam scanning electron microscope (FIB-SEM) at the Open

University, equipped with an Oxford Instruments INCA energy dispersive X-ray detector. The same instrument includes a Deben Centaurus CL panchromatic detector with Hamamatsu Photo Multiplier Tube (model R316), with a spectral response in 400–1200 nm region. The electron beam generated with an acceleration voltage of 15–20 kV and a current of 0.52–0.62 nA, under a working distance of 15 mm was used for generation of SE and BSE images, as well as for acquisition of energy dispersive spectra (EDS). The phosphate grains were located in each thin section using elemental EDS X-ray mapping, which revealed P-hotspots. In this way, we were able to locate even the grains that are as small as a few micrometers. A dwell time of 100 ms per step was used. To distinguish between apatite and merrillite based on the presence of F and Cl in apatite, Mg in merrillite and relative Ca signal, as well as to evaluate the petrographic context of the phosphates, we used point analysis (Point and ID) with ~20 s live-time spectrum acquisition per point. SEM-based CL imaging is sensitive to internal textures, defects, trace element distribution, and zoning in plagioclase and phosphates (Götze and Kempe 2008). In this study, it was applied to investigate the microtexture of minerals in order to estimate their shock level. CL imaging was performed on selected phosphate and plagioclase grains, using a working distance of ~13 mm, 7–10 kV, and 0.7–1.2 nA.

Electron Backscatter Diffraction

Lattice orientation, internal microtexture, and structural disorder of selected apatites and merrillites were studied by EBSD. After SEM analyses, isopropanol and, if needed, 0.25 μm diamond paste were used for removing carbon coat from the samples. Subsequently, the thin sections were lightly polished for approximately 10 min using either 50 nm alumina or colloidal silica of 0.06 μm water suspension with a Buehler Vibromat II vibratory polisher (University of Portsmouth) or LabPol-5 system with a LabForce-1 head and an automated doser at the Open University, to ensure the removal of surface defects. This process minimizes scatter of the electron beam due to surface interaction and is a critical step for accurate microstructural analysis by EBSD.

Target phosphate grains were identified using X-ray elemental maps of the thin section. Micro- to nano-scale structural analysis was conducted by EBSD using an Oxford Instruments Nordlys EBSD detector mounted on a Zeiss EVO MA10 LaB_6-SEM housed at the University of Portsmouth. Diffracted electrons were collected at a tilt angle of 70°, at 100–300 nm step size with collection times <120 ms per step (e.g., White et al. 2017). Generated apatite diffraction patterns were matched to a hexagonal unit cell using crystal lattice parameters of (Wilson et al. 1999) $a = 9.4555$, $b = 9.4555$, $c = 6.8836$, and $\alpha = 90°$, $\beta = 90°$, $\gamma = 120°$. Merrillite was indexed against a trigonal symmetry (Xie et al. 2015), with parameters of $a = 10.3444$, $b = 10.3444$, $c = 37.0182$, $\alpha = 90°$, $\beta = 90°$, $\gamma = 120°$. The interaction volume for diffracted electrons using these parameters is estimated to be a few tens of nanometers in width and depth (Darling et al. 2016). Diffraction patterns were automatically captured and indexed every 50–200 nm across a manually defined area. Raw patterns are automatically background corrected during acquisition, removing an averaged 64 frames of "noise" from each pattern. Wild spike reduction was conducted on all data set, though no other form of raw data correction was conducted. Complete instrument parameters are presented in Table S1 in supporting information. A total of ~30 apatite and merrillite grains were analyzed in this study, and the representative grains are presented in Figs. 3–5, and S3 in supporting information.

Raman Spectroscopy

Internal structural disorder of plagioclase, apatite, and merrillite was also investigated by Raman spectroscopy. Analyses were performed at the Open University using a HORIBA Jobin Yvon HR800 system equipped with 473 nm (blue diode), 514 nm (green Ar^+), and 632 nm (red HeNe) excitation lasers. Because of repolishing of the samples, it was relatively easy to locate the grains under the reflected light, thus, the optical focus was used for optimizing analyses. Individual point spectra were collected using 632.8 nm excitation wavelength, choosing 150 μm slit and 300 μm hole size, with a 600 g/mm grating and 800 mm focal length spectrometer, achieving a spectral resolution of approximately 3 cm^{-1}. Spectra were accumulated as three sets of 20–60 s integrations to improve the signal-to-noise ratio. Low laser power of up to ~5 mW at the sample surface when using 50% filters, was aimed throughout all measurements, to minimize thermal damage to the sample. However, it was decreased to 10% filter when analyzing the most heavily shocked and deformed minerals, when it was needed to better resolve spectral features due to the high background (fluorescence). An estimated minimal spatial resolution of ~1.54 μm of the laser beam was achieved on the sample's surface when using 50× objective with 0.5 numerical aperture, calculated based on equation of spectral resolution = 1.22*λ/numerical aperture, as given in the Horiba manufacturer's manuals (http://www.horiba.com/scientific/products/raman-spectroscopy/raman-academy/raman-faqs/what-analysis-spot-or-laser-spot-

size-is-used-for-a-raman-microscope/). The spectral range was calibrated using a silicon standard (520.7 ± 0.5 cm^{-1}) at the beginning of each analytical session, in order to determine the accuracy of the spectral position and the intensity of the scattered beam. The calibration file is automatically used by the acquisition software LabRam software v.6. when acquiring the spectra. Characteristic peaks in the spectra were processed in the range 200–1200 cm^{-1}, corrected for a polynomial baseline in LabRam software v. 6. and fitted assuming Lorentzian peak shapes.

RESULTS

Estimates of Shock-Level Stages in Samples Based on Plagioclase Deformation

In this study, we focused on mafic rocks, comprised of plagioclase and orthopyroxene as the main mineral constituents. Plagioclase is readily deformed by shock and is a useful mineral to evaluate stages of shock deformation using existing calibration (Stöffler et al. 1991; Rubin et al. 1997; Fritz et al. 2017). Based on optical properties, progressive stages of plagioclase shock deformation were categorized following the scale revised and modified by Fritz et al. (2017), initially proposed by Stöffler et al. (1991) and extended by Rubin et al. (1997). The optical observations were then complemented using SEM-CL panchromatic imaging and Raman spectroscopy, as they were recently shown to be useful tools in recognizing shock-induced features (Fernandes et al. 2013; Russell et al. 2014; Pernet-Fisher et al. 2017). We also inspected shock stages of orthopyroxene, as it is the only other major mineral in these rocks.

Troctolite 76535

Optical investigation of plagioclase in the polished section 76535,51 shows pristine magmatic texture and twinning, with sharp optical extinction. Orthopyroxene in this rock also shows no signs of shock deformation. SEM-CL images (Figs. 1a and 1b) and accompanying Raman spectra (Fig. 2), in accordance with the optical images, do not reveal any signs of microstructural complexities in plagioclase. All major peaks of anorthite are present (283, 487, 506, and 560 cm^{-1}), in agreement with literature data (e.g., RUFF anorthite X050020; Xie et al. 2017). Hence, this troctolite is assigned a deformation stage equivalent to S1 (<5 GPa) following existing calibrations.

Anorthositic Troctolite 76335

Within the polished section of cataclastic anorthositic troctolite (76335,60), both plagioclase and orthopyroxene show signs of shock deformation. Plagioclase is mechanically fragmented and fractured,

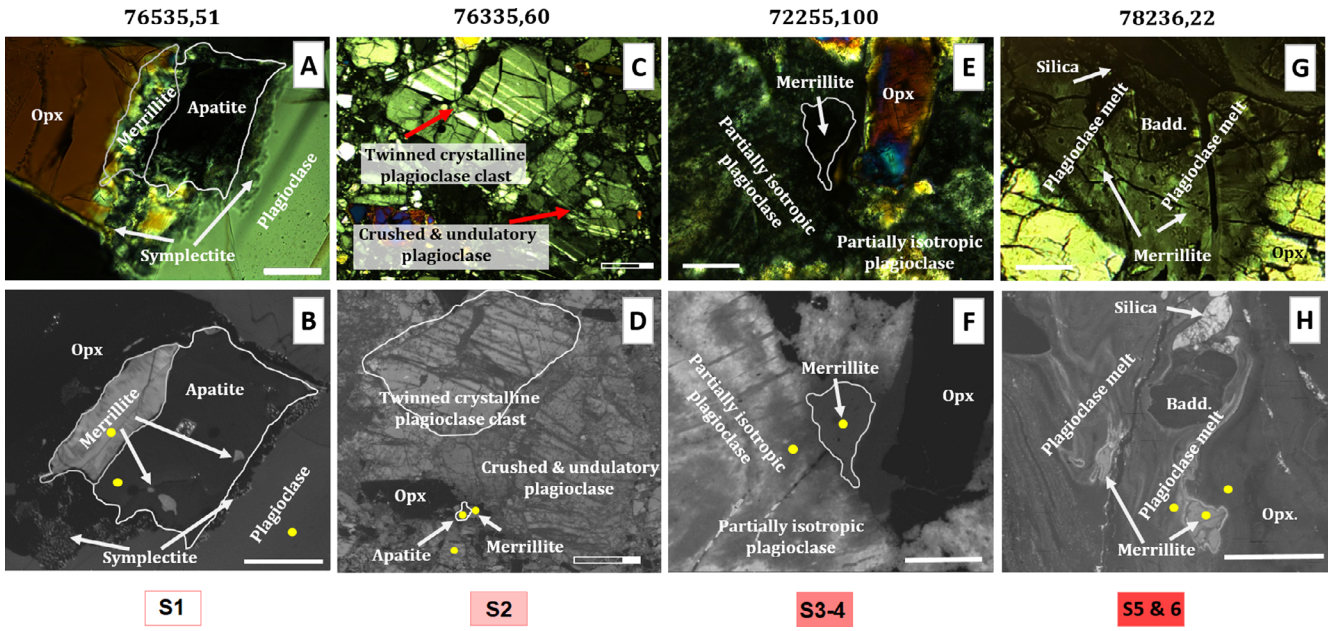

Fig. 1. Optical (upper panels) and cathodoluminescence (lower panels) images of analyzed rocks, showing plagioclase, apatite, and merrillite at different stages of shock deformation (S1–S6). All scale bars are 50 μm, including the white bars in C and D, which are also extended to 200 μm for better clarity. Yellow dots in the CL panel indicate the position of the acquired Raman spectra presented in Fig. 2. (Color figure can be viewed at wileyonlinelibrary.com.)

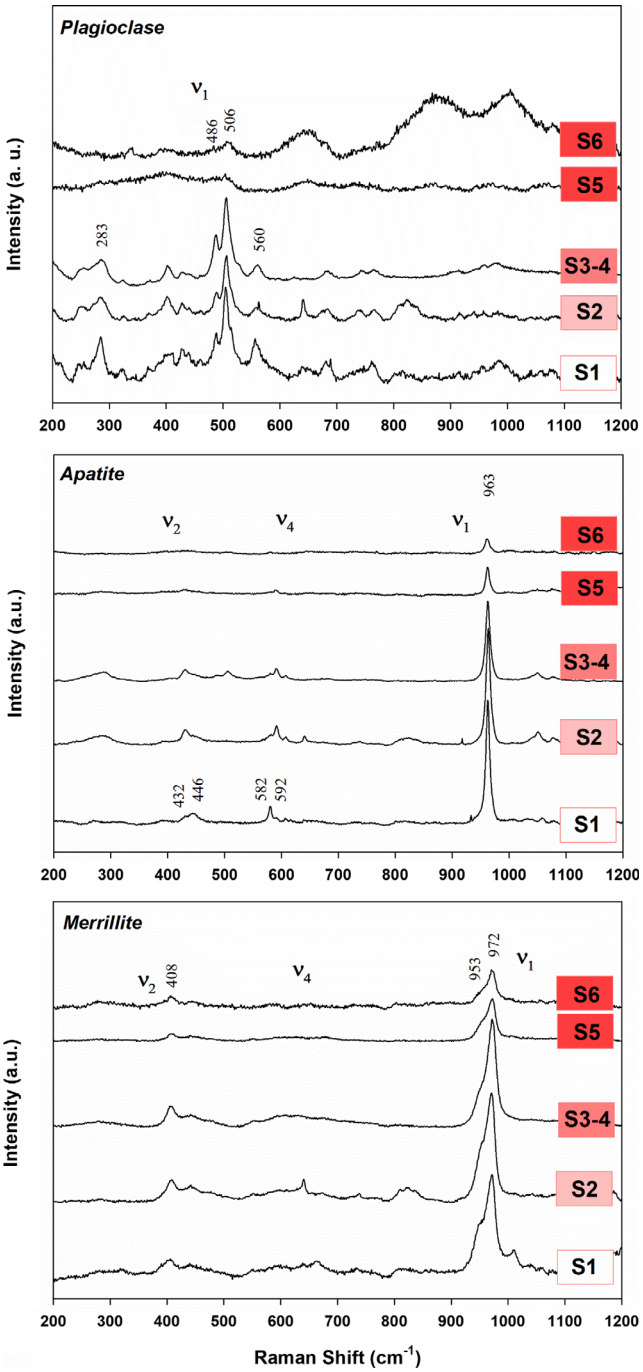

Fig. 2. Raman spectra of plagioclase, apatite, and merrillite obtained for samples displaying different shock stages and indicated by yellow dots in Fig. 1. Main vibration modes are annotated. Peak fitting parameters of all individual spectra except for plagioclase at S5 and S6 are given in Table S2 in supporting information, labelled by individual mineral and its shock stage. All individual spectra are provided in the supporting information (Color figure can be viewed at wileyonlinelibrary.com.)

with no evidence of dynamic recrystallization. However, three apparent forms (Figs. 1c and 1d) of plagioclase displaying different stages of deformation are observed in this sample, including (1) coarse irregular fragments showing very good crystallinity; (2) less coarse plagioclase fragments that show decrease in birefringence, possibly indicating early stages of amorphization (e.g., Jaret et al. 2014); these fragments mostly surround the larger crystalline clasts, possibly marking the original grain size. The size of these plagioclase fragments gradually decreases toward the very fine grains in the matrix; (3) very fine-grained (<1 μm) plagioclase in the matrix of this rock, which appears darker in plane polarized light and remains consistently dark under crossed polars. The less coarse and the very fine-grained plagioclase appear mottled and smeared under reflected light. Orthopyroxene is heavily fractured too; however, not fragmented to the same extent as plagioclase, showing only initial signs of undulatory extinction. SEM-CL imaging of large crystalline plagioclase fragments shows mostly undisturbed interior and good crystallinity (Fig. 1d). The CL signal of smeared plagioclase and the fine-grained matrix is much brighter, most likely reflecting the surface effect and enhanced grain boundaries rather than intracrystalline defects. SEM-based CL imaging is very sensitive to the fine-scale surface appearance, and although depth of beam penetration is commonly 2–8 μm (Reed 2005), the variations may arise from atypical surfaces (Kempe et al. 2000; Kempe and Gotze 2002). However, the mechanically crushed plagioclase could also host a number of crystalline defects that would contribute to higher CL response (Gucsik et al. 2005).

Raman spectroscopy does not indicate any difference in crystallinity between three different forms of plagioclase, depicting that even the fine-grained matrix shows a well-developed Raman spectrum that likely indicates well-homogenized powder of randomly oriented small plagioclase crystallites. Also, the overall quality of the Raman spectrum does not indicate any significant drop in the number of prominent peaks, nor in their shape or intensity, revealing that the crystallinity of cataclastic plagioclase in 76335,60 is comparable to that of plagioclase in 76535,51 troctolite. Interestingly, the alternating magmatic twins within large crystalline fragments of plagioclase, evident under crossed polars, depict differences in the CL signal. These twins do not show any difference in composition, as both show equally low Na content. Closer inspection of the twins does not reveal obvious signs of selective deformation, no differences in optical relief, and no differences in birefringence or in the Raman signal, as described before (Jaret et al. 2014). Moreover, the darker set of twins displays short inclusions that are aligned along the twin plane (Fig. S1 in supporting information), as opposed to inclined lamellae in alkali

feldspar, which are found to be perpendicular to the twinning plane (Jaret et al. 2014). The phenomenon of variable CL intensity in differently oriented crystals (twins) was earlier reported in studies on lunar minerals by Sippel and Spencer (1970) and reviewed by Götze (2009). According to the comparative barometry of major phases (Stöffler et al. 1991; Rubin et al. 1997; Fritz et al. 2017), the troctolite 76335 is deformed at stage S2 (~5–10 GPa), as evident from the lack of progressive plagioclase deformation.

Civet Cat *Norite Fragment 72255*

The major constituents in the polished section of *Civet Cat* norite (72255,100) display evidence of severe shock deformation (Figs. 1e and 1f). In plane polarized light, both plagioclase and orthopyroxene appear mottled. We find that most of the plagioclase grains are still partially birefringent and only rarely completely isotropic (Fig. 1e), interpreting it to be evidence of partially diaplectic plagioclase and the onset of isotopization. Orthopyroxene is fractured, displaying mosaicism and patchy extinction, occasionally also kink-bend structures. Anorthite endmember of plagioclase is expected to transform to diaplectic glass at ~20–24 GPa (Fritz et al. 2005). The Ca-endmember requires lower shock pressure to transform to diaplectic glass than the alkali-feldspars, most likely due to the fact that it contains more Al-O bonds, which are weaker and can endure less confining pressure than Si-O bonds (Stöffler et al. 1986; Fritz et al. 2005, 2017). This is in contrast with the fact that anorthite has a higher bulk modulus (0.94 Mbar) than alkali-feldspars (e.g., albite 0.7 Mbar), which reflects its higher incompressibility (Angel et al. 1988). CL imaging of the partially isotropic plagioclase returns strong signal and displays spongy appearance of plagioclase grains (Fig. 1f). Most grains display textural zoning, with very bright rims and darker cores. Similar rim features were earlier documented in plagioclase from Dhofar 081 meteorite (Russell et al. 2014). The dominant CL activator in lunar plagioclase is Mn^{2+} (560 nm in M site) due to its common substitution with Ca^{2+} (Götze 2009; Götze et al. 2015). It was reported that the CL response in this spectral region increases with increasing An content of plagioclase (Götze 2009), which conforms well with the fact that the plagioclase of *Civet Cat* is highly anorthitic (Bersch et al. 1991). Another intense source of CL activation arises from the substitution of Al^{3+} and Si^{4+}, causing a local Al-O^{-}-Al defect. A contributor to CL activation in plagioclase, in the 400–900 nm region can also be rare earth elements. Due to the limitation of panchromatic SEM-CL imaging, we could not determine the exact wavelength of the CL spectrum; however, we can conclude that the zoning in *Civet Cat* plagioclase could be related either to trace element content of plagioclase (e.g., REEs) or to higher density of defects in the rim region, or a combination of both. We exclude the possibility of variable An content, based on previous studies that showed homogeneity of minerals in this clast (Ryder et al. 1975; Bersch et al. 1991). A reaction rim in the form of absorbed grain boundaries can be observed toward associated orthopyroxene grains, indicating possible postshock re-equilibration of the rock that could have triggered trace element mobility. Also, a high number of μm-sized metal droplets are concentrated in plagioclase rim and grain boundary region, highlighting a possible reaction front. A slight decrease in the intensity of most Raman peaks is observed; however, the most prominent A_g doublet does not show any signs of intensity drop or peak broadening. This is similar to the previous observation by Fritz et al. (2005) for partially birefringent plagioclase that experience deformation at a pressure slightly below that needed for diaplectic glass formation (26–32 GPa). The norite fragment 72255,100 has experienced shock levels at stages S3–S4 (15–35 GPa) as evident from an incomplete diaplectic glass formation.

Shocked Norites 78235 and 78236

Shock features in 78235,43 and 78236,22 norite were extensively studied since the earliest work on Apollo samples (El Goresy et al. 1976), and were found to display different grades of shock metamorphism, indicating an inhomogeneous distribution of shock pressures and postshock temperatures. Plagioclase records deformation stages ranging from subordinate birefringent cores, to formation of plagioclase diaplectic glass to regions of melted plagioclase glass in the grain rim and particularly in relation to grain boundaries with orthopyroxene (Figs. 1g and 1h), in agreement with early observations (Jackson et al. 1975; Sclar and Bauer 1975; El Goresy et al. 1976). The orthopyroxene is heavily brecciated and displays mosaicism, undulatory extinction, and shock lamellae. We observe moderate CL response of the diaplectic glass, and very strong CL activation of plagioclase melted glass in the form of very bright patches and flow features (schlieren) (Fig. 1h). This is in contrast to the observation by Pernet-Fisher et al. (2017), who reported no activation of diaplectic glass in the CL spectrum. However, our finding is in agreement with other studies (e.g., Kayama et al. 2012). The very bright CL response is most likely caused by high density of defects within diaplectic glass and plagioclase melted glass, as it was previously reported that no chemical zoning was observed within them. The Raman spectra of diaplectic and melted plagioclase glass were recorded in this study (Fig. 2).

Due to high luminescence, it was not possible to collect Raman spectra of the brown impact melt. The changes in the spectral features that occur in the diaplectic glass compared to plagioclase are in agreement with Fritz et al. (2005), Fernandes et al. (2013), and Xie et al. (2017). General degradation of the spectra quality, decrease in number of peaks and their intensity, as well as increased luminescence evidence the S5 deformation stage. The most prominent doublet in the 480–505 cm^{-1} region is barely visible, resulting from a loss of the long-range periodicity in the structure of diaplectic glass (Figs. 2 and S5 in supporting information). A broad peak at ~650 cm^{-1} and a doublet as 900–1000 cm^{-1} of the spectra sampling melted plagioclase glass are in agreement with Xie et al. (2017) and indicate the highest S6 stage of shock-induced deformation (Fig. 2). This rock has undoubtedly experienced an overall exposure to shock pressures > 35 GPa (S5) due to broad conversion of plagioclase to diaplectic glass, with local maxima reaching > 60 GPa (S6), where incipient melting of plagioclase occurred and melt veins are formed.

Cathodoluminescence, Raman Spectroscopy, and EBSD Characterization of Shocked Lunar Apatite and Merrillite

The size of the phosphate minerals (commonly < 100 μm), requires high-resolution techniques for inspection of their microstructures. In this study, two SEM-based techniques, EBSD and CL imaging, were coupled with Raman spectroscopy to provide complementary structural analysis of the phosphates. All investigated grains are apatite and merrillite of primary origin, preserved in the pristine, albeit shock-metamorphosed, Mg-suite mineral assemblages (primarily plagioclase and orthopyroxene with subordinate clinopyroxene, silica, baddeleyite, and other accessory minerals). Apatite and merrillite are commonly spatially associated. EDS mapping revealed ~5–10 suitable apatite in each thin section, with the largest grains having ~50 μm in the longest dimension. All apatite and merrillite have anhedral grain shape, mostly showing subequant crystal habit.

Merrillite appears brighter in most of the SEM-CL images than apatite (Figs. 1 and S4 in supporting information). The main activator of the CL in apatite is Mn^{2+}, visible as a broad peak in 500–600 nm region (Götze 2009). Trace amounts of REEs can also activate CL in the region from 300 to 900 nm (e.g., Götze 2009; Aldave et al. 2011). On the other hand, Fe^{2+} is reported as the main quencher of the CL signal in most lunar minerals (Götze and Kempe 2008; Götze 2009). Most of the investigated apatite contain trace amounts of FeO (e.g., Barnes et al. 2014, 2016), that could be contributing to the duller signal of apatite. Although EPMA cannot reveal the speciation of iron, it is reasonable to suspect that at least a portion of it in lunar apatite is Fe^{2+}, due to very low oxygen fugacity on Moon. Merrillite in the studied rocks contains ~12 wt% of REEs (Barnes et al. 2014), which are the main contributor to the CL signal in this mineral. Higher CL activation in merrillite over apatite has been reported previously (Aldave et al. 2011; Ashcroft et al. 2017).

The Raman spectra of apatite and merrillite collected in the region 200–1200 cm^{-1}, indicate generally good crystallinity of the grains at all stages of shock deformation, however, with significant weakening of the bands at stages S5 and S6 (Fig. 2). The strongest Raman band in apatite is located at 963 cm^{-1} (see Table S2 for peak fitting parameters), in agreement with literature values for dominantly but not pure fluorapatite composition (e.g., Rruff database R040098), and also in agreement with anion composition reported for highlands Mg-suite apatite (~3 wt% F and ~1 wt% Cl; Barnes et al. 2014). This bend corresponds to the ν_1 symmetric stretch of the PO_4 tetrahedra. Other minor bending modes are visible in the 400–600 cm^{-1} region. The most intense ν_1 symmetric stretch in merrillite is present as a weak doublet of peaks located at 953 and 972 cm^{-1}. The Raman spectrum of merrillite from other planetary samples show well-defined doublet (e.g., Xie et al. 2002; Jolliff et al. 2006; Aldave et al. 2011); however, all reported Raman spectra of lunar merrillite contain a weak doublet or a highly asymmetric single peak (Jolliff et al. 1996, 2006). The difference in the peak shape of the ν_1 vibration is attributed to the high REE content unique to lunar merrillite (Jolliff et al. 2006). Other Raman bands in merrillite are well-developed, too, but are of significantly lower intensity. The bands with frequencies in the 1080–1100 cm^{-1} region correspond to the ν_3 asymmetric-stretching vibration; the bands recorded at frequencies in the 400–500 cm^{-1} and 550–660 region correspond to the ν_2 and ν_4 bending modes, respectively. The vibrations and fluorescence related to REEs are expected at frequencies higher than 1200 cm^{-1}, outside of the spectral region collected in this study.

The EBSD data set includes high-resolution (100–500 nm step size) maps of 15 apatite and 11 merrillite grains. Data are analyzed and displayed as band contrast (BC) images, texture component (TC) maps, and as inverse pole figures (IPF). BC images account for the overall state of crystallinity, TC maps reveal internal misorientation of individual grains, and IPFs reproduce the crystallographic orientation of the individual crystals.

Shock-Induced Microtextures in Apatite and Merrillite

Shock Stage S1

Troctolite 76535 experienced minimal shock loading. Two apatite and two merrillite grains were inspected in this sample. Apatite and merrillite are in contact with plagioclase and orthopyroxene, which show no evidence of shock metamorphism. Both types of phosphates form large single crystals in this rock and seem undisturbed in CL images (Fig. 1). The CL signal of merrillite is much brighter than that of apatite and also that of the surrounding plagioclase, most likely activated by the high content of REEs (~12 wt %; Barnes et al. 2014). Content of Mn, an important CL activator in apatite in this sample is reported to be very low, below detection limits (Barnes et al. 2014), therefore probably not contributing to the CL activation. However, as this rock contains a significant KREEP component, apatite is enriched in REEs, which are probably causing the CL signal in apatite. Barnes et al. (2014) reported low Ce and high Y content of apatite, whereby the latter can be considered as a proxy for HREE due to their similar ionic radii.

The Raman spectrum of apatite and merrillite indicates well-crystallized grains, with no signs of structural disorder (Fig. 2). The ν_1 symmetric stretching bend in merrillite is rather a weak doublet at 953 cm^{-1} and 972 cm^{-1} than an asymmetric single peak reported for other lunar lithologies (Jolliff et al. 2006). Merrillite in the studied polished section (76535,51) probably contains slightly more HREEs, as indicated by high Y_2O_3 content (Barnes et al. 2014) and less Ce_2O_3 and other LREEs compared to the merrillite studied before (Jolliff et al. 2006). A difference in REE content may cause the difference in the ν_1 peak shape (Jolliff et al. 2006). See Table S2 for the apatite and merrillite Raman spectra peak fitting parameters. As revealed by BC maps (Figs. 3 and 4), apatite and merrillite at S1 stage show very high crystallinity, with no signs of microscopic deformation. Apatite displays mechanical fragmentation into large individual fragments that are slightly misoriented to each other, as can be seen on the IPF panel with highlighted grain boundaries (GB) (Fig. 3). Individual fragments are large (~20-50 μm), separated by long and slightly curved GBs that are indicating < 20° misorientation between individual fragments, thus retaining the overall orientation uniform across the apatite grain (see IPF). Merrillite does not show any fragmentation, with some local aggregation of low-angle (>1° but < 10°) GBs (Fig. 4). Individual fragments of apatite and the merrillite grain show no more than 2–3° of internal crystal-plastic deformation (CPD), as revealed by the TC maps (Figs. 3 and 4, TC panel), and also demonstrated in pole figures (Figs. 3 and 4, pole figures panel).

Shock Stage S2

Shock deformation displayed in the polished section of troctolite 76335,60 involves cataclastic deformation, mechanical breaking, and crushing of all the minerals, including apatite and merrillite. Seven apatite and three merrillite grains were inspected in this sample. BC imaging shows that both apatite and merrillite underwent early-stage, subgrain formation of several μm in size, with typically irregular subgrain boundaries (Figs. 3 and 4, BC panel). While apatite mostly shows low-angle GBs (>1° but < 10°), merrillite appears more prone to subgrain formation and often displays subgrains of random relative orientation with either a lobate or a grid-like network of subgrain boundaries that can reach > 60° (Fig. 4, IPF panel with GB). Merrillite subgrain size visibly decreases and the density of low-angle GBs increases with increasing mechanical deformation of the merrillite grain (Fig. 4, IPF panel with GB). The either lobate or grid-like texture of the subgrains suggests that the subgrain formation is more likely a response to general crushing of the rock rather than an intrinsic microtexture of the mineral and therefore difficult to separate from fragmentation. It is potentially triggered by increased heating provided by the impact. However, individual fragments or subgrains remain minimally deformed (2-3° of CPD), as revealed by the texture component maps (Fig. 4, TC panels). CL imaging of apatite and merrillite does not resolve any subgrains or microtextural complexities. CL signal of merrillite is much stronger than that of apatite, and its brightness is similar to that of the surrounding plagioclase (Fig. 1). Raman spectra of apatite and merrillite at S2 deformation stage do not look any different from those at S1 (Fig. 2), revealing well crystalline material with no signs of structural disorder (Table S2).

Shock Stage S3-4

Apatite and merrillite within *Civet Cat* clast are mostly surrounded with anorthitic plagioclase, and only sporadically in contact with orthopyroxene. Three apatite and one merrillite grain were inspected in this section. The BC of both phases appears darker than at S1 and S2, suggesting a decrease in crystallinity. At this stage, subgrain formation is very prominent in both apatite and merrillite (Figs. 3 and 4, BC panel), with the size of individual subgrains being 1–5 μm, and increased density of irregular low-angle GBs. Only occasionally, GBs reach > 20° and are associated with differently oriented fragments. In case of apatite, the high-angle GBs are mostly associated with the fragmentation of apatite into the top and the bottom half, which can be best

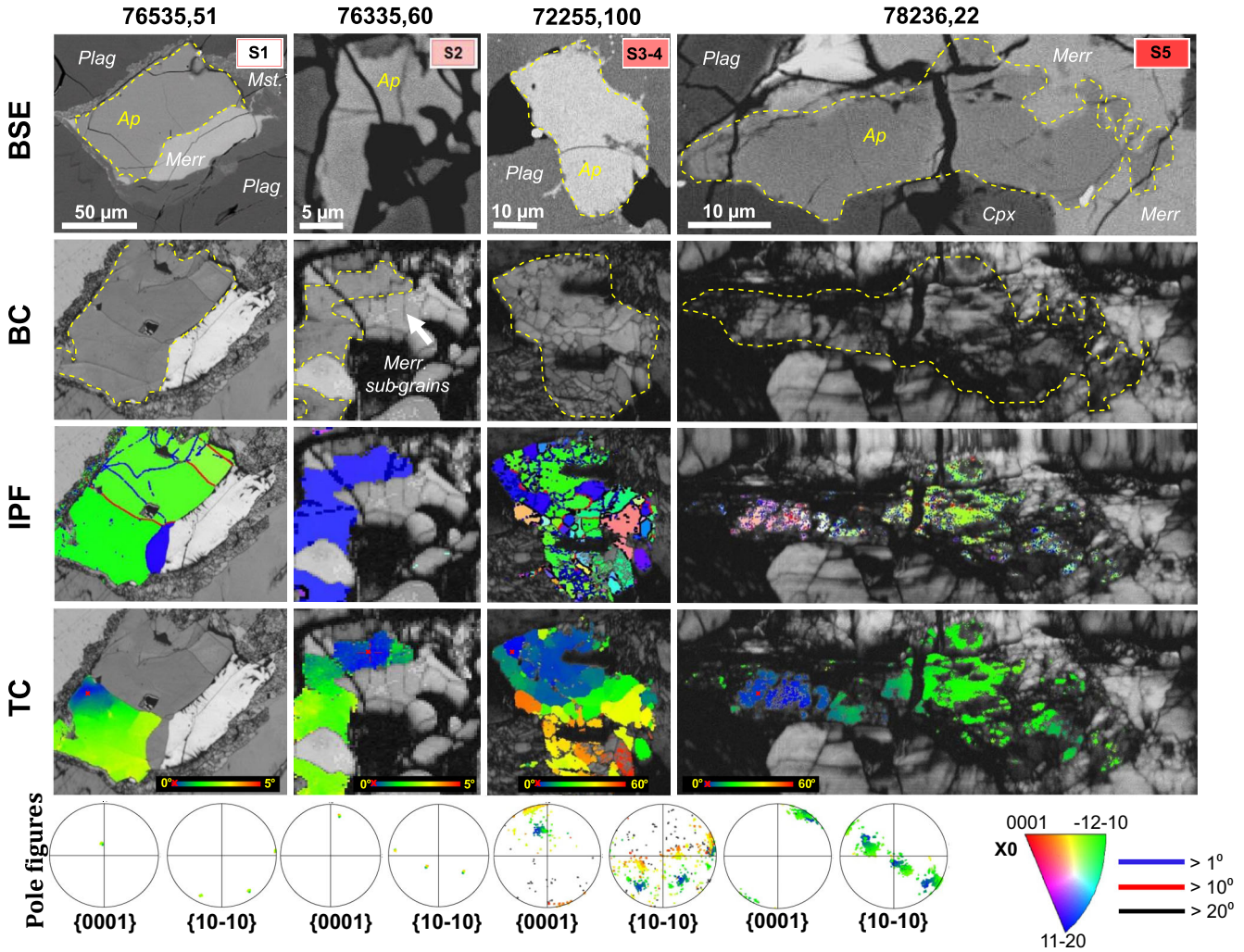

Fig. 3. Backscatter electron (BSE), band contrast (BC), inverse pole figures (IPF) including grain boundaries, and texture component (TC) maps of apatite grains that have experienced deformation from S1 to S5 stages. The lowest panel shows pole figures corresponding to the TC maps. Yellow dashed line in BSE and BC panels is outlying studied apatite grain. BSE images clearly indicate individual fragments of apatite (e.g., S1) but do not reveal any internal complexities of the apatite structure that occur as response to increasing shock-loading (S2 and higher), easily picked up by BC maps. BC maps show that subgrain formation becomes more prominent, reducing the subgrain size with increasing shock-loading. The IPF figures that indicate severity of internal deformation at stages >S2, are color-coded based on the guide in the bottom right corner. Grain boundaries are presented along with IPF. TC maps can be used to quantify internal, crystal-plastic deformation (CPD) of individual grains, i.e., fragments (two individual fragments in case of S3–S4) of apatite, and show up to 25°CPD at S5. (Color figure can be viewed at wileyonlinelibrary.com.)

understood by looking at TC and pole figures (Fig. 3). In the case of merrillite, the high-angle GBs are associated with few external subgrains (Fig. 4). Internal deformation across domains of subgrains separated by low-angle GBs yields up to ~10° of CPD in apatite and up to ~12° in merrillite, a sign of significant lattice deformation of individual crystals, visible in the pole figures, too (Figs. 3 and 4, TC and pole figure panels). Interestingly, CL signal of merrillite is very similar to that of apatite and appears dull compared to the bright signal of surrounding plagioclase (Figs. 1e and 1f). CL signal in apatite indicates weak irregular zoning with areas inside the grain showing slightly brighter CL signal, possibly arising from an increased density of low-angle GBs and defects. CL image of merrillite indicates very homogenous interior. Raman spectra of phosphates at shock stage S3-S4 imply weakening of the signal and an overall quality decrease (Fig. 2). In both minerals, the main ν_1 symmetric stretch is less intense, albeit the full width at half maximum (FWHM) does not indicate any peak broadening (Table S2), and therefore represents no significant reduction in crystallinity.

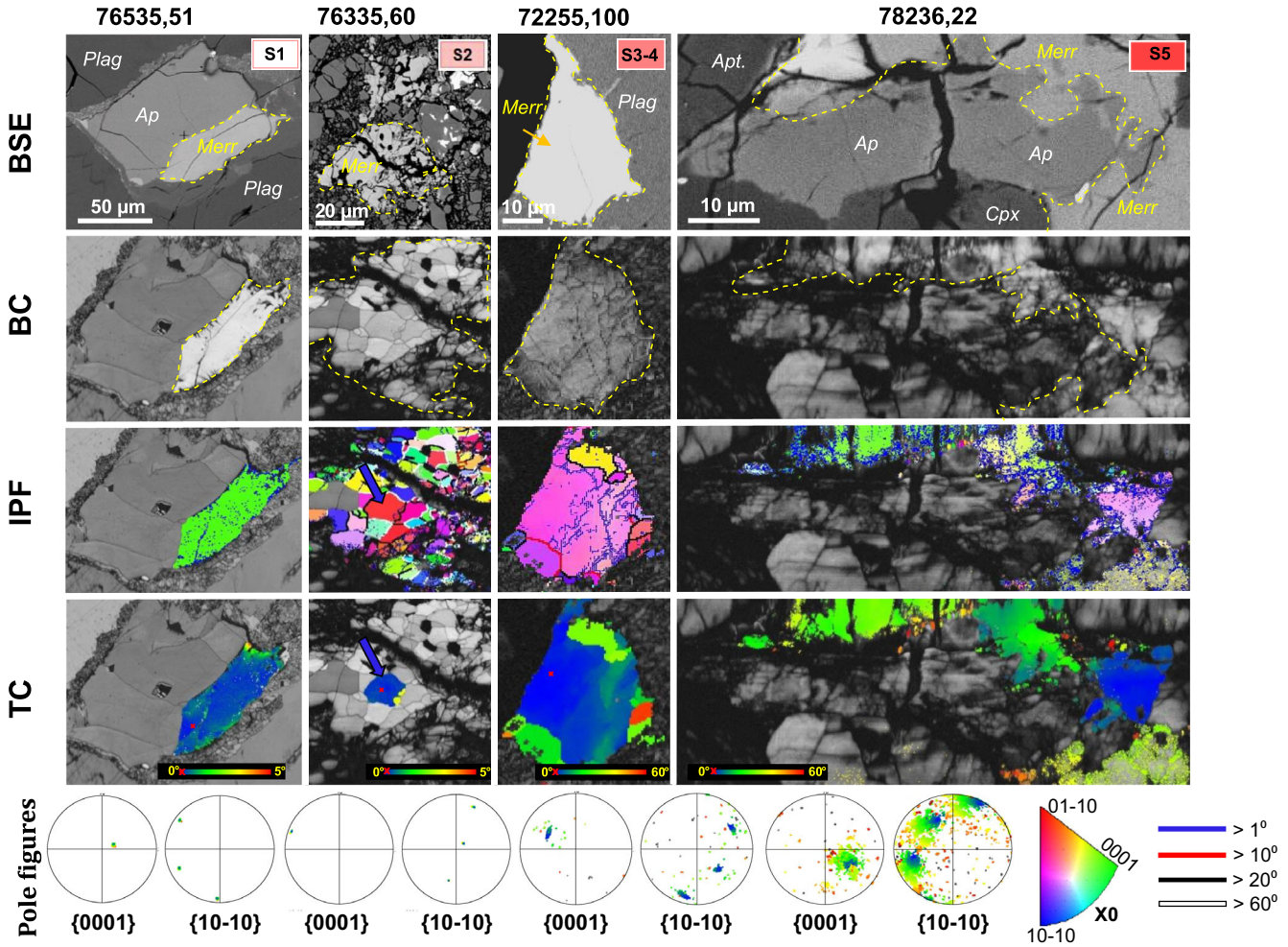

Fig. 4. Backscatter electron (BSE), band contrast (BC), inverse pole figures (IPF) including grain boundaries, and texture component (TC) maps of merrillite grains that have experienced deformation from S1 to S5 stages. The lowest panel shows pole figures corresponding to the TC maps. Yellow dashed line in BSE and BC panels is outlying studied merrillite grain. BSE images clearly indicate individual fragments of merrillite (e.g., S2) but do not reveal any internal complexities of the that occurs due to the shock-loading (S2 and higher). BC maps, on the other hand, show that subgrain formation becomes more prominent at S2 and higher, reducing the subgrain size with increasing shock-loading. The IPF figures indicate severity of internal deformation at stages >S2 and are color-coded based on the guide in the bottom right corner. Grain boundaries are presented along with IPF. TC maps are used to quantify internal, crystal-plastic deformation (CPD) of individual grains, i.e., fragments (e.g., at S2) of merrillite and show up to 30° CPD at S5. (Color figure can be viewed at wileyonlinelibrary.com.)

Shock Stage S5

Apatite and merrillite are in contact with both diaplectic plagioclase and melted plagioclase glass, but also with minerals that have higher shock impedance than plagioclase, i.e., are less prone to deformation (orthopyroxene, clinopyroxene). Five apatite and three merrillite grains were imaged at S5 stage. BC imaging of an apatite in contact with orthopyroxene and clinopyroxene (S5) reveals an interior dominated by subgrains that are < 1 µm and appear poorly diffracting at the length scales of EBSD (~tens of nm), surrounding ~10 µm sized clasts of preserved crystallinity (Fig. 3, BC panel). The preserved clasts record significant crystal-plastic deformation, as evident from increased density of very short (sub-µm) low-angle GBs, accumulated mostly toward the rim of the clasts and in contact with poorly diffracting material (Fig. 3, IPF panel with GBs). High-angle GBs > 20° are uncommon, and those < 20° but > 10° are occasionally present. Texture component maps show up to 25° of misorientation across what appears to be one single grain of apatite in BSE image and across the indexed portions of the grains, evidence of severe crystal-plastic deformation (Fig. 3, TC and pole figure panels). While these grains are heavily deformed, no signs of recrystallization of apatite are obvious at this scale. All apatites and

merrillites observed in 78235 and 78236 samples show equally extreme deformation (Fig. S3). Merrillite associated with orthopyroxene and subordinate clinopyroxene (S5) also appears dominated by poorly diffracting subgrains surrounding highly deformed clasts. Extensive crystal lattice deformation of up to 30° across the entire indexable grain is observed (Fig. 4, TC and pole figure panels). In both minerals, CL features show lighter cloudy regions in the areas indexed with lower crystallinity by EBSD, indicating a high density of defects (Fig. S4). Raman spectra of phosphates associated with orthopyroxene and clinopyroxene complement the EBSD pattern by indicating that material is mostly well crystallized despite poorly diffracting EBSD patterns, albeit showing evidence of structural disorder and overall signal weakening compared to lower deformation stages. Apatite and merrillite associated with orthopyroxene and clinopyroxene are assigned with S5 stage of deformation, as they show evidence of severe shock deformation, with no evidence of melting or recrystallization at this scale.

Shock Stage S6

Within heavily shocked norite 78235 and 78236, we also find phosphates associated with diaplectic plagioclase glass and impact melt (Figs. 1g and 1h). The grains found in contact with diaplectic and melted plagioclase glass show more pervasive shock deformation than the phosphates "protected" by the high-impedance phases such as orthopyroxene and clinopyroxene. Four apatite and three merrillite grains were inspected at S6 stage. Apatite found in contact with diaplectic glass, melted plagioclase, and impact melt shows very weak diffraction in EBSD, such that no successful indexing of any such grain was possible. The Raman spectrum of apatite related to diaplectic glass and impact melt (Figs. 2 and S6 in supporting information) shows further weakening compared to S5 that, albeit very weak, still preserves the ν_1 band, indicating that at least a portion of the grain retains its crystallinity. On the other hand, EBSD imaging of merrillite associated with diaplectic glass, melted plagioclase, and impact melt revealed a very complex and granular interior (see BC, TC maps and the pole figure in Fig. 5), much coarser than the interior of the grain at S5 (Fig. 4). The BC maps of the granular interior of merrillite imply that at least a portion of it has a very good crystallinity and that at least partial recrystallization of the grain could have taken place. High-angle GBs (Fig. S5) associated with the granular interior are more common than in previously described grains; however, the low-angle GBs are dominant and there appears to be a prevailing crystallographic orientation in the TC map and pole figures (Fig. 5), suggesting that the recrystallization was following the crystallographic orientation of the precursor grain. The EBSD pattern additionally revealed very fine-grained crystallites surrounding merrillite that can be indexed as anorthite, suggesting that plagioclase melt and diaplectic glass form very fine crystallites, too (Fig. S5). The Raman spectrum of this particular melt also suggests that recrystallization is taking place (Fig. 5). Raman spectra of merrillite associated with diaplectic glass and/or plagioclase melt look very similar to S5, suggesting that they are of the same crystallinity. Interestingly, EBSD indexing of recrystallized merrillite was equally successfully performed when using unit cell parameters of the high-pressure polymorph tuite, however, no such polymorph was confirmed by Raman spectroscopy. Apatite and merrillite grains associated with diaplectic glass, melted plagioclase, and impact melt are assigned with S6 stage of shock deformation as they record the highest level of deformation observed in this sample.

DISCUSSION AND IMPLICATIONS

Shock-Barometry Based on Major Minerals

More energetic impacts were required to launch rocks off the Moon (and Mars), than off Vesta, so about 30% of lunar basaltic meteorites are rich in diaplectic glass and melted plagioclase glass (Rubin 2015). However, diaplectic glass and melted plagioclase glass are very rarely found among Apollo samples, which qualifies them as suitable candidates for studying deformation induced by lower shock pressures. Moreover, in the context of studying effects of shock-loading, Apollo rocks are ideal because they are unaffected by terrestrial alteration that could potentially modify indigenous lunar signatures. Direct assessment of shock deformation in plagioclase and other major minerals using optical microscopy is well documented in the literature, and provides proven and refined shock deformation scales (Stöffler 1971; Stöffler et al. 1986, 1991; Rubin et al. 1997; Goresy et al. 2008; Jaret et al. 2014; Pickersgill et al. 2015). However, Raman spectroscopy is not as straightforward in this respect, especially in the lower end pressure regime (e.g., Fritz et al. 2005). The Raman spectroscopy measurements carried out in this study are in agreement with a previous study (Fritz et al. 2005) showing a slight overall decrease in the quality of the Raman spectra and peak fitting parameters with increasing pressure (Table S2). The differences are most striking at pressures at which diaplectic glass and plagioclase melted glass form (S4 and higher, >20 GPa); however, they remain negligible in spectra from the lower stages

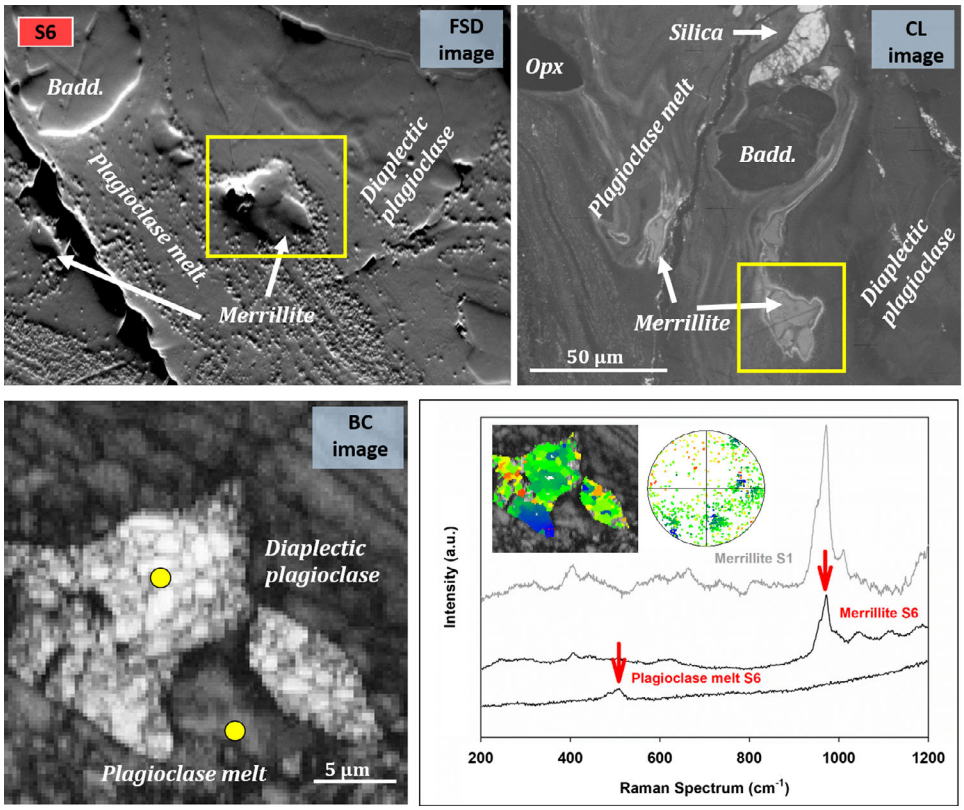

Fig. 5. Recrystallization of merrillite at S6 surrounded by diaplectic and melted plagioclase glass (78236,22). Forward-scatter diffraction (FSD) image enhances surface features revealing low relief of the phosphate, high and granular surface of the plagioclase melt in contrast to the flat surface of diaplectic plagioclase. Band contrast (BC) image yields very good crystallinity of granular merrillite, and lower crystallinity of surrounding fine-grained melted plagioclase glass (see supporting information for TC map). Raman spectra collected at annotated yellow spots depict weak ν1 stretching mode in both phases. Raman spectrum of merrillite at S1 in 76535,51 (gray line) is given for intensity comparison. Inset above the Raman spectrum represents a TC map of the recrystallized merrillite and the corresponding pole figure. The recrystallization is not entirely random and it most likely follows the original crystal orientation. (Color figure can be viewed at wileyonlinelibrary.com.)

(Fig. 2). This sets the limits on the applicability of Raman spectroscopy in shock deformation assessment at lower pressures, which are particularly prevalent among Apollo samples. The Raman spectroscopy can only be used as comparative means in the assessment of shock deformation, provided that samples which experienced a range of deformation stages are available for investigation. Unlike Raman spectroscopy, the panchromatic SEM-CL imaging is sensitive to internal textures, defects, trace element distribution, and zonal growth of plagioclase (Götze and Kempe 2008). The depth of penetration of the luminescence effect is commonly 2–8 µm (Reed 2005) but variations may arise from atypical surface appearance (Kempe et al. 2000), which is very useful for studying brecciated shocked rocks (e.g., cataclastic troctolite 76335). SEM-CL imaging obtained in this study demonstrated high practicality of the method for assessing shock stages of plagioclase deformation. SEM-CL imaging is an excellent complementary tool to assess the level of shock deformation in plagioclase, additionally allowing an insight into the internal structure, as well as into the relation with surrounding minerals. Although orthopyroxene is a useful coexisting mineral for shock assessment of Mg-suite lunar rocks using optical microscopy, it does not exhibit any CL activation, presumably because of CL quenching effect on account of its high iron content (Götze 2009).

Accessory Mineral Shock-Barometry and its Implications

Apatite and merrillite are often small accessory phases that cannot be optically inspected for evidence of shock deformation. However, the microtextural state of the two minerals may play an essential role when interpreting in situ age data, as previously demonstrated for other accessory minerals (e.g., Erickson et al. 2015; Kovaleva and Klötzli 2017; Kovaleva et al. 2017).

However, phases such as titanite (Papapavlou et al. 2018) and monazite (Erickson et al. 2017) display only local domains of age resetting, making them useful though situational impact chronometers. For the mineral zircon ($ZrSiO_4$), complete resetting of the U-Th-Pb systematics only occurs in recrystallized neoblastic domains (Cavosie et al. 2015; Kenny et al. 2017, 2019a), the formation of which appears to be restricted to the high-temperature impact melt sheet environment. The formation of micrometer-scale {112} twins, indicative of shock pressures in excess of ~18 GPa (Moser et al. 2011), induce only partial disturbance of Pb (Cavosie et al. 2015), while planar deformation features, formed at ~10 GPa, do not facilitate Pb loss (Moser et al. 2011). As a result, zircon is a less-than-ideal shock chronometer, with only the most extreme P–T conditions yielding fresh impact age subdomains. Given the large variations in closure temperatures for Pb diffusion in apatite (450–550 °C; Cherniak et al. 1991; or as high as 620 °C in larger grains, Krogstad and Walker 1994) and zircon (>900 °C; Cherniak 2010), and the relatively high intensity of CPD observed here in phosphate minerals, the phase should be particularly susceptible to Pb diffusion and loss during postimpact annealing and crater modification, as previously observed at the Nicholson Lake impact structure (McGregor et al. 2018). Due to the elevated (~400 °C) closure temperature of Pb in apatite, the resetting of the Pb-Pb geochronometer is to expect in rocks that have experienced at least mild heating, for example, rocks that are in contact with impact melt but not necessarily affected by high-temperature modifications. Hence, the resetting is likely to occur also in rocks that do not undergo plagioclase modification to diaplectic glass. We, thus, suggest based on our microtextural study that apatite is likely to be a particularly sensitive impact chronometer and should be a target of future efforts to date bombardment events in planetary materials and terrestrial impact structures.

Although BSE imaging provides a good scale for observation of these minerals, it does not reveal any signs of internal textural complexities and, therefore, cannot be used to assess microtexture of the grains. Our EBSD analyses of apatite and merrillite reveal a well-developed record of microtextural changes in course of increasing shock-loading that can discriminate S1 to S6 stages of shock deformation in lunar samples. These changes involve subgrain formation without an apparent decrease in the crystallinity of the mineral at lower shock stages, followed by decrease in subgrain size and increase in crystal-plastic deformation (up to >25° at S6), accompanied by a decrease in crystallinity. It should be noted, however, that the extreme CPD observed in lunar apatite and merrillite is associated with shock deformation solely based on the nature and the history of the sample but it can be expected to occur in other geologic settings, as well. For example, a high CPD was documented in zircon from a shear zone (Kovaleva and Klötzli 2017; Kovaleva et al. 2017). Based on the texture components maps, it was suspected that an intermediate level of deformation between stages S2 and S3 (expected CPD 3°–8°) exists; however, it was not present in the studied samples. Furthermore, we did not observe any deformation twin lamellae, which occur as a result of shock deformation in many terrestrial accessory minerals (xenotime, zircon, or monazite), in either of the phosphates. We did, however, observe planar fractures in apatite at S6 deformation (in 78235) that are similar to those described earlier in apatite from terrestrial impact structures (Cavosie and Centeno 2014; McGregor et al. 2018). Also, the apatite observed in *Civet Cat* norite (S3-4) shows granular microtexture similar to that reported by Kenny et al. (2019a).

Raman spectroscopy and SEM-CL imaging of phosphates proved to be a useful tool for targeting best grain candidates for further EBSD inspection; however, it demonstrated significant limitations. Comparable to that of plagioclase, Raman signal of apatite and merrillite shows abrupt change at S4 and higher, but it remains almost undisturbed at lower pressure scale. Equally, the panchromatic CL signal of apatite and merrillite indicates first signs of intergranular complexities at very high pressures. Among all applied techniques, we find EBSD to yield the most diagnostic and quantitative measure of microtextural changes related to the shock-induced deformation of lunar phosphates. A summary of different diagnostic features of plagioclase, apatite, and merrillite obtained using three different techniques is outlined in Table 1. For comparison, at S3-S4, both merrillite and apatite show significant microtextural response to shock loading that can be well-quantified (Figs. 3 and 4), whereas plagioclase deformation at the same stage can only be observed optically and inferred from the weakening of the Raman mode.

Merrillite shows lower shock impedance than apatite, i.e., more deformation at the same shock level. This behavior could be a reflection of the compressibilities of the two minerals. The zero-pressure isothermal bulk modulus of apatite of comparative composition is K_{T0} = 91.5(38) GPa (Matsukage et al. 2004). The K_{T0} of merrillite rich in REEs has not been reported so far, but it can be compared to that of synthetic whitlockite of pure $Ca_3(PO_4)_2$ composition, which is reported to be slightly lower than that of apatite K_{T0} = 79(2) GPa (Zhai and Wu 2010). In this respect, it is expected that merrillite compression is higher compared to that of apatite at the same pressure. Neither of these minerals were observed to

Table 1. Summary of shock-induced features at different shock stages, as revealed by different analytical techniques.

Mineral		S1	S2	S3–4	S5	S6
	Method:					
Plagioclase	Raman	Well-developed	Well-developed	Slight weakening	Weakening	Loss
	CL	Homogenous	Surface enhanced contrast	Spongy—texture	Patches & flow features	Patches & flow features
Apatite	Raman	Well-developed	Well-developed	Slight weakening	Weakening	Weakening
	CL	Homogenous	Homogenous	Slight zoning	Irregular zoning	Homogenous
	EBSD	Homogenous; well-diffracting; 2°–3° CPD	Well-diffracting; subgrain formation; 2°–3° CPD	Enhanced subgrain formation; severe CPD up to 10°	Enhanced sub-grain formation; severe CPD up to 25°	No diffraction
Merrillite	Raman	Well-developed	Well-developed	Slight weakening	Weakening	Weakening
	CL	Homogenous	Homogenous	Slight zoning	Irregular zoning	Homogenous
	EBSD	Homogenous; well-diffracting; 2°–3° CPD	Well-diffracting; subgrain formation; 2°–3° CPD	Enhanced subgrain formation; severe CPD up to 12°	Enhanced subgrain formation; severe CPD up to 30°	Evident recrystallization

CL = cathodoluminescence; CPD = crystal-plastic deformation; EBSD = electron backscatter diffraction.

undergo any phase transformations below approximately 15 GPa (Xie et al. 2003).

The evidence of microstructural changes in response to shock metamorphism of these widely used accessory minerals should be taken into account when interpreting their crystallization ages, as it was shown in other accessory minerals that differently shocked domains can yield significantly different ages (e.g., Erickson et al. 2015; Darling et al. 2016; Kovaleva and Klötzli 2017; Kovaleva et al. 2017). For example, a complex set of phosphate ages measured in Chelyabinsk meteorite could be related to the fact that the phosphates in this meteorite are clearly different in terms of their microtextures, which suggests their nonsynchronous formation or deformation (Walton et al. 2018). Future research should focus more on the effects of complex apatite microstructures on the distribution and abundance of volatile species. If volatile species and their isotopes vary on the same order of magnitude as age reservoirs, then such features could substantially alter water abundance and D/H isotopic ratios, important aspects of understanding the origin of water in the solar system.

CONCLUSION

Stages of deformation ranging from S1 (no shock deformation) to S6 are described in a set of Apollo 17 Mg-suite samples, based on the level of shock deformation of the associated plagioclase. Microtextures in apatite and merrillite are progressively more complex and deformed with increasing levels of shock-loading. An early shock-stage fragmentation at S2, is followed by subgrain formation at S3-S4, further decrease in subgrain size with increasing deformation (S5), and finally with granularization (recrystallization) at the S6 (Table 1). Starting with 2–3° of intragrain crystal-plastic deformation in both phosphates, apatite undergoes up to 25° and merrillite up to 30° of crystal-plastic deformation at the highest stage of shock deformation (S5), before recrystallization takes place (S6). Merrillite displays lower shock impedance than apatite, hence it is more deformed at the same level of shock-loading.

Electron backscatter diffraction technique is demonstrated to be a reliable, nondestructive technique that provides a direct insight into the microtexture of the phosphates, delivering maps that are easy to quantify. In the case of phosphates, EBSD can be guided or complemented, but not replaced by Raman spectroscopy or SEM-CL imaging due to the insufficient insight provided by the latter two techniques. However, SEM-CL is demonstrated to be particularly useful for visualization of shock-deformed plagioclase.

We suggest that the microtexture of apatite and merrillite visualized by EBSD should be routinely inspected when asserting the overall stage of shock deformation of the rock, particularly when interpreting in situ geochemically relevant information obtained from the phosphates, such as age or volatile content, as it has been shown in other accessory minerals (e.g., zircon, monazite, xenotime, and baddelyite) that differently deformed domains can yield significantly different ages.

Acknowledgments—We thank NASA CAPTEM for allocation of Apollo samples. MA and AC acknowledge funding from the European Union's Horizon 2020 research and innovation program under grant agreement no. 704696 (Marie Skłodowska Curie fellowship to AC). This research was partially supported by a STFC grant to MA (# ST/L000776/1 and ST/P000665/1). Pete Landsberg and Geoff Long are kindly acknowledged for their assistance in sample polishing. Diane Johnson is thanked for her help with SEM and CL work. The authors are grateful to two anonymous reviews for their constructive comments that improved this manuscript. We thank Katherine Joy for the editorial handling of the manuscript.

Editorial Handling—Dr. Katherine Joy

REFERENCES

Adcock C., Tschauner T. O., Hausrath E. M., Udry A., Luo S. N., Cai Y., Ren M., Lanzirotti A., Newville M., Kunz M., and Lin C. 2017. Shock-transformation of whitlockite to merrillite and the implications for meteoritic phosphate. *Nature Communications* 8:14667.

Aldave L. A., Guinea J. G., and Tormo L. 2011. Spectra luminescence of extraterrestrial calcium phosphates in Mexican chondrites. *Spectroscopy Letters* 44:574–579.

Alwmark C., Wouter B., Anthony L., Laurence P., and Anders S. 2017. An early ordovician 40Ar-39Ar age for the ~50 Km carswell impact structure, Canada. *GSA Bulletin* 129:1442–1449.

Anand M. 2014. Analyzing Moon rocks. *Science* 344:365–366.

Anand M., Tartèse R., and Barnes J. J. 2014. Understanding the origin and evolution of water in the Moon through lunar sample studies. *Philosophical Transactions of the Royal Society of London A: Mathematical, Physical and Engineering Sciences* 372:20130254.

Angel R., Hazen R., Mccormick T., Prewitt C., and Smyth J. 1988. Comparative compressibility of end-member feldspars. *Physics and Chemistry of Minerals* 15:313–318.

Ashcroft H. A., Anand M., Franchi I. A., Johnson D., and Černok A. 2017. Inter- and intra-crystalline geochemical and textural variations of apatites in two Apollo 12 basalts. In *5th European Lunar Symposium*, Muenster, Germany.

Barnes J. J., Tartèse R., Anand M., McCubbin F. M., Franchi I. A., Starkey N. A., and Russell S. S. 2014. The origin of water in the primitive Moon as revealed by the lunar highlands samples. *Earth and Planetary Science Letters* 390:244–252.

Barnes J. J., Tartèse R., Anand M., McCubbin F. M., Neal C. R., and Franchi I. A. 2016. Early degassing of lunar urKREEP by crust-breaching impact(s). *Earth and Planetary Science Letters* 447:84–94.

Barrett T. J., Barnes J. J., Tartèse R., Anand M., Franchi I. A., Greenwood R. C., Charlier B. L. A., and Grady M. M. 2016. The abundance and isotopic composition of water in eucrites. *Meteoritics & Planetary Science* 51:1110–1124.

Baziotis I. P., Liu Y., DeCarli P. S., Jay Melosh H., McSween H. Y., Bodnar R. J., and Taylor L. A. 2013. The Tissint Martian meteorite as evidence for the largest impact excavation. *Nature Communications* 4:1404.

Bellucci J. J., Whitehouse M. J., John T., Nemchin A. A., Snape J. F., Bland P. A., and Benedix G. K. 2017. Halogen and Cl isotopic systematics in Martian phosphates: Implications for the Cl cycle and surface halogen reservoirs on Mars. *Earth and Planetary Science Letters* 458:192–202.

Bersch M. G., Taylor G. J., Keil K., and Norman M. D. 1991. Mineral compositions in pristine lunar highland rocks and the diversity of highland magmatism. *Geophysical Research Letters* 18:2085–2088.

Borg L. E., Connelly J. N., Cassata S. W., Gaffney A. M., Carlson R., Papanastassiou D., Wasserburg J., Ramon E., Lindval R., and Bizzarro M. 2013. Evidence for widespread magmatic activity at 4.36 Ga in the Lunar Hughlands from young ages determined on troctolite 76535 (abstract #1563). 44th Lunar and Planetary Science Conference, CD-ROM.

Borg L. E., Connelly J. N., Cassata S. W., Gaffney A. M., and Bizzarro M. 2017. Chronologic implications for slow cooling of troctolite 76535 and temporal relationships between the Mg-suite and the Ferroan anorthosite suite. *Geochimica et Cosmochimica Acta, Isotopic Studies of Planetary and Nuclear Materials: A Scientific Tribute to Ian Douglass Hutcheon (1947-2015)* 201:377–391.

Boyce J. W., Liu Y., Rossman G. R., Guan Y., Eiler J. M., Stolper E. M., and Taylor L. A. 2010. Lunar apatite with terrestrial volatile abundances. *Nature* 466:466–469.

Boyce J. W., Tomlinson S. M., McCubbin F. M., Greenwood J. P., and Treiman A. H. 2014. The lunar apatite paradox. *Science* 344:400–402.

Bruand E., Fowler M., Storey C., and Darling J. 2017. Apatite trace element and isotope applications to petrogenesis and provenance. *American Mineralogist* 102:75–84.

Carlson R. W., Borg L. E., Gaffney A. M., and Boyet M. 2014. Rb-Sr, Sm-Nd and Lu-Hf isotope systematics of the lunar Mg-suite: The age of the lunar crust and its relation to the time of Moon formation. *Philosophical Transactions of the Royal Society of London A: Mathematical, Physical and Engineering Sciences* 372:20130246.

Cavosie A. J. and Centeno C. L. 2014. Shocked apatite from the Santa Fe impact structure (USA): A new accessory mineral for studies of shock metamorphism (abstract #1691). 45th Lunar and Planetary Science Conference. CD-ROM.

Cavosie A. J., Erickson T. M., Timms N. E., Reddy S. M., Talavera C., Montalvo S. D., Pincus M. R., Gibbon R. J., and Moser D. 2015. A terrestrial perspective on using ex situ shocked zircons to date lunar impacts. *Geology* 43:999–1002.

Cavosie A. J., Montalvo P. E., Timms N. E., and Reddy S. M. 2016. Nanoscale deformation twinning in xenotime, a new shocked mineral, from the Santa Fe impact structure (New Mexico, USA). *Geology* 44:803–806.

Cherniak D. J. 2010. Diffusion in accessory minerals: Zircon, titanite, apatite, monazite and xenotime. *Reviews in Mineralogy and Geochemistry* 72:827–869.

Cherniak D. J., Lanford W. A., and Ryerson F. J. 1991. Lead diffusion in apatite and zircon using ion implantation and Rutherford backscattering techniques. *Geochimica et Cosmochimica Acta* 55:1663–1673.

Chew D. M. and Spikings R. A. 2015. Geochronology and thermochronology using apatite: Time and temperature, lower crust to surface. *Elements* 11:189–194.

Compston W., Foster J. J., and Gray C. M. 1975. Rb-Sr ages of clasts from within Boulder 1, Station 2, Apollo 17. *The Moon* 14:445–462.

Darling J. R., Moser D. E., Barker I. R., Tait K. T., Chamberlain K. R., Schmitt A. K., and Hyde B. C. 2016. Variable microstructural response of baddeleyite to shock metamorphism in young basaltic shergottite NWA 5298 and improved U-Pb dating of solar system events. *Earth and Planetary Science Letters* 444:1–12.

Dymek R. F., Albee A. L., and Chodos A. A. 1975. Comparative petrology of lunar cumulate rocks of possible primary origin: Dunite 72415, troctolite 76535, norite 78235, and anorthosite 62237. Proceedings, 6th Lunar Science Conference. pp. 301–341.

Economos R., Boehnke P., and Burgisser A. 2017. Sulfur isotopic zoning in apatite crystals: A new record of dynamic sulfur behavior in magmas. *Geochimica et Cosmochimica Acta* 215:387–403.

Edmunson J., Nyquist L. E., and Borg L. E. 2007. Sm-Nd isotopic systematics of troctolite 76335 (abstract #1962). 38th Lunar and Planetary Science Conference. CD-ROM.

Edmunson J., Borg L. E., Nyquist L. E., and Asmerom Y. 2009. A combined Sm–Nd, Rb–Sr, and U-Pb isotopic study of Mg-suite norite 78238: Further evidence for early differentiation of the Moon. *Geochimica et Cosmochimica Acta* 73:514–527.

Edmunson J., Cohen B. A., Carpenter P., Zeigler R. A., and Jolliff B. L. 2010. Yttrium silicate in lunar troctolitic anorhtosite 76335 (abstract #2627). 41st Lunar and Planetary Science Conference. CD-ROM.

El Goresy A., Engelhardt W. von, Arndt J., and Manglier D. 1976. Shocked norite 78235: Primary textures and shock features (abstract). 7th Lunar Science Conference. pp. 239–241.

Erickson T. M., Pearce M. A., Taylor R. J. M., Timms N. E., Clark C., Reddy S. M., and Buick I. S. 2015. Deformed monazite yields high-temperature tectonic ages. *Geology* 43:383–386.

Erickson T. M., Timms N. E., Kirkland C. L., Tohver E., Cavosie A. J., Pearce M. A., and Reddy S. M. 2017. Shocked monazite chronometry: Integrating microstructural and in situ isotopic age data for determining precise impact ages. *Contributions to Mineralogy and Petrology* 172:11.

Fernandes V. A., Fritz J., Weiss B. P., Garrick-Bethell I., and Shuster D. L. 2013. The bombardment history of the Moon as recorded by ^{40}Ar-^{39}Ar chronology. *Meteoritics & Planetary Science* 48:241–269.

Flicoteaux R. and Lucas J. (1984). Weathering of phosphate minerals. In *Phosphate minerals*, edited by Nriagu J. O. and Moore P. B. Berlin: Springer. pp. 292–317.

Fritz J., Greshake A., and Stöffler D. 2005. Micro-Raman spectroscopy of plagioclase and maskelynite in Martian meteorites: Evidence of progressive shock metamorphism. *Antarctic Meteorite Research* 18:96.

Fritz J., Greshake A., and Fernandes V. A. 2017. Revising the shock classification of meteorites. *Meteoritics & Planetary Science* 52:1216–1232.

Göpel C., Manhès G., and Allègre C. J. 1994. U-Pb systematics of phosphates from equilibrated ordinary chondrites. *Earth and Planetary Science Letters* 121:153–171.

Goresy A. E., Dera P., Sharp T. G., Prewitt C. T., Chen M., Dubrovinsky L., Wopenka B., Boctor N. Z., and Hemley R. J. 2008. Seifertite, a dense orthorhombic polymorph of silica from the Martian meteorites Shergotty and Zagami. *European Journal of Mineralogy* 20:523–528.

Götze J. 2009. Cathodoluminescence microscopy and spectroscopy of lunar rocks and minerals. In *Cathodoluminescence and its application in the planetary sciences*, edited by Gucsik A. Berlin: Springer. pp. 87–110.

Götze J. and Kempe U. 2008. A comparison of optical microscope- and scanning electron microscope-based cathodoluminescence (CL) imaging and spectroscopy applied to geosciences. *Mineralogical Magazine* 72:909–924.

Götze J., Habermann D., Kempe U., Neuser R. D., and Richter D. K. 2015. Cathodoluminescence microscopy and spectroscopy of plagioclases from lunar soil. *American Mineralogist* 84:1027–1032.

Greenwood J. P., Itoh S., Sakamoto N., Warren P., Taylor L., and Yurimoto H. 2011. Hydrogen isotope ratios in lunar rocks indicate delivery of cometary water to the Moon. *Nature Geoscience* 4:79–82.

Gucsik A., Nishido H., Ninagawa K., Toyoda S., Bidló A., Brezsnyánszky K., and Tsuchiyama A. 2005. Cathodoluminescence spectral studies of the experimentally shock-deformed plagioclase: A possible explaination of CL peak shifts (abstract #1239). 36th Lunar and Planetary Science Conference. CD-ROM.

Harlov D. E. 2015. Apatite: A fingerprint for metasomatic processes. *Elements* 11:171–176.

Heiken G. H., Vaniman D. T., and French B. M. 1991. Lunar sourcebook—A user's guide to the Moon. http://adsabs.harvard.edu/abs/1991lsug.book....H. Accessed March 16, 2018.

Hinthorne J. R., Conrad R. L., and Church S. E. 1977. Leadlead age and rare earth element determinations in lunar norite 78235 (abstract). 8th Lunar Science Conference. pp. 444–446.

Hughes J. M. 2015. The many facets of apatite. *American Mineralogist* 100:1033–1039.

Hughes J. M. and Rakovan J. 2002. The crystal structure of apatite, $Ca_5(PO_4)_3(F, OH, Cl)$. *Reviews in Mineralogy and Geochemistry* 48:1–12.

Hughes J. M., Jolliff B. L., and Gunter M. E. 2006. The atomic arrangement of merrillite from the Fra Mauro Formation, Apollo 14 lunar mission: The first structure of merrillite from the Moon. *American Mineralogist* 91:1547–1552.

Hughes J. M., Jolliff B. L., and Rakovan J. 2008. The crystal chemistry of whitlockite and merrillite and the dehydrogenation of whitlockite to merrillite. *American Mineralogist* 93:1300–1305.

Ionov D. A., Hofmann A. W., Merlet C., Gurenko A. A., Hellebrand E., Montagnac G., Gillet P., and Prikhodko V. S. 2006. Discovery of whitlockite in mantle xenoliths: Inferences for water- and halogen-poor fluids and trace element residence in the terrestrial upper mantle. *Earth and Planetary Science Letters* 244:201–217.

Jackson E. D., Sutton R. L., and Wilshire H. G. 1975. Structure and petrology of a cumulus norite boulder sampled by Apollo 17 in Taurus-Littrow valley, the Moon. *Geological Society of Ameica Bulletin* 86:433–442.

Jaret S. J., Kah L. C., and Harris R. S. 2014. Progressive deformation of feldspar recording low-barometry impact processes, Tenoumer impact structure, Mauritania. *Meteoritics & Planetary Science* 49:1007–1022.

Johnson J. R. 2012. Thermal infrared spectra of experimentally shocked andesine anorthosite. *Icarus* 221:359–364.

Johnson J. R., Hörz F., Lucey P. G., and Christensen P. R. 2002. Thermal infrared spectroscopy of experimentally shocked anorthosite and pyroxenite: Implications for remote sensing of Mars. *Journal of Geophysical Research: Planets* 107:3-1–3-14.

Jolliff B. 2014. Merrillite and apatite as recorders of planetary magmatic processes. *American Mineralogist* 99:2161–2162.

Jolliff B. L., Haskin L. A., Colson R. O., and Wadhwa M. 1993. Partitioning in REE-saturating minerals: Theory, experiment, and modelling of whitlockite, apatite, and evolution of lunar residual magmas. *Geochimica et Cosmochimica Acta* 57:4069–4094.

Jolliff B. L., Freeman J. J., and Wopenka B. 1996. Structural comparison of Lunar, terrestrial and synthetic whitlockite using laser raman microprobe spectroscopy (abstract #613). 27th Lunar and Planetary Science Conference. CD-ROM

Jolliff B. L., Hughes J. M., Freeman J. J., and Zeigler R. A. 2006. Crystal chemistry of lunar merrillite and comparison to other meteoritic and planetary suites of whitlockite and merrillite. *American Mineralogist* 91:1583–1595.

Jones R. H., McCubbin F. M., Dreeland L., Guan Y., Burger P. V., and Shearer C. K. 2014. Phosphate minerals in LL chondrites: A record of the action of fluids during metamorphism on ordinary chondrite parent bodies. *Geochimica et Cosmochimica Acta* 132:120–140.

Jones R. H., Mccubbin F. M., and Guan Y. 2016. Phosphate minerals in the H group of ordinary chondrites, and fluid activity recorded by apatite heterogeneity in the Zag H3-6 regolith breccia. *American Mineralogist* 101:2452–2467.

Kayama M., Nishido H., Sekine T., Nakazato T., Gucsik A., and Ninagawa K. 2012. Shock barometer using cathodoluminescence of alkali feldspar. *Journal of Geophysical Research-Planets* 117:E09004.

Kempe U. and Gotze J. 2002. Cathodoluminescence (CL) behaviour and crystal hemistry of apatite from rare-metal deposits. *Mineralogical Magazine* 66:135–156.

Kempe U., Gruner T., Nasdala L., and Wolf D. 2000. Relevance of cathodoluminescence for the interpretation of U-Pb zircon ages, with an example of an application to a study of zircons from the Saxonian Granulite Complex, Germany. In *Cathodoluminescence in geosciences*, edited by Pagel M., Barbin V., Blanc P., and Ohnenstetter D. Berlin: Springer Verlag. pp. 425–456.

Kenny G. G., Morales L. F., Whitehouse M. J., Petrus J. A., and Kamber B. S. 2017. The formation of large neoblasts in shocked zircon and their utility in dating impacts. *Geology* 45:1003–1006.

Kenny G. G., Schmieder M., Whitehouse M. J., Nemchin A., Morales L. F., Buchner E., Belluci J. J., and Snape J. F. 2019a. A new U-Pb age for shock-recrystallised zircon from the Lappajarvi impact crater, Finland, and implications for the accurate dating of impact events. *Geochimica et Cosmochimica Acta* 245:479–494.

Kenny G. G., Andreas Karlsson A., Schmieder M., Whitehouse M. J., Nemchin A. A., and Bellucci J. J. 2019b. A Review of shock-metamorphic features in apatite from terrestrial impact structures and possible implication for extra-terrestrial phosphates (abstract #1357). 50th Lunar and Planetary Science Conference. CD-ROM.

Konecke B. A., Fiege A., Simon A. C., Parat F., and Stechern A. 2017. Co-variability of S6 + , S4 + , and S2− in apatite as a function of oxidation state: Implications for a new oxybarometer. *American Mineralogist* 102:548–557.

Kovaleva E. and Klötzli U. 2017. NanoSIMS study of seismically deformed zircon: Evidence of Y, Yb, Ce, and P redistribution and resetting of radiogenic Pb. *American Mineralogist* 102:1311–1327.

Kovaleva E., Klötzli U., Habler G., Huet B., Guan Y., and Rhede D. 2017. The effect of crystal-plastic deformation on isotope and trace element distribution in zircon: Combined BSE, CL, EBSD, FEG-EMPA and NanoSIMS study. *Chemical Geology* 450:183–198.

Krogstad E. J. and Walker R. J. 1994. High closure temperatures of the U-Pb system in large apatites from the Tin Mountain pegmatite, Black Hills, South Dakota, USA. *Geochimica et Cosmochimica Acta* 58:3845–3853.

Leich D. A., Kahl S. B., Kirschbaum A. R., Niemeyer S., and Phinney D. 1975. Rare gas constraints on the history of Boulder 1, Station 2, Apollo 17. *The Moon* 14:407–444.

Mao M., Rukhlov A. S., Rowins S. M., Spence J., and Coogan L. A. 2016. Apatite trace element compositions: A robust new tool for mineral exploration. *Economic Geology* 111:1187–1222.

Matsukage K. N., Ono S., and Kawamoto T. 2004. The compressibility of a natural apatite. *Physics and Chemistry of Minerals* 31:580–584.

McCubbin F. M. and Jones R. H. 2015. Extraterrestrial apatite: Planetary geochemistry to astrobiology. *Elements* 11:183–188.

McCubbin F. M., Steele A., Hauri E. H., Nekvasil H., Yamashita S., and Hemley R. J. 2010. Nominally hydrous magmatism on the Moon. *Proceedings of the National Academy of Sciences* 107:11,223–11,228.

McCubbin F. M., Shearer C. K., Burger P. V., Hauri E. H., Wang J., Elardo S. M., and Papike J. J. 2014. Volatile abundances of coexisting merrillite and apatite in the Martian meteorite Shergotty: Implications for merrillite in hydrous magmas. *American Mineralogist* 99:1347–1354.

McCubbin F. M., Vander Kaaden K. E., Tartèse R., Klima R. L., Liu Y., Liu Y., Mortimer J., Barnes J. J., Shearer C. K., Treiman A. H., and Elardo S. M. 2015. Magmatic volatiles (H, C, N, F, S, Cl) in the lunar mantle, crust, and regolith: Abundances, distributions, processes, and reservoirs. *American Mineralogist* 100:1668–1707.

McGregor M., McFarlane C. R. M., and Spray J. G. 2018. In situ LA-ICP-MS apatite and zircon U-Pb geochronology of the Nicholson Lake impact structure, Canada: Shock and related thermal effects. *Earth and Planetary Science Letters* 504:185–197.

Merle R. E., Nemchin A. A., Grange M. L., Whitehouse M. J., and Pidgeon R. T. 2014. High resolution U-Pb ages of Ca-phosphates in Apollo 14 breccias: Implications for the age of the Imbrium impact. *Meteoritics and Planetary Science* 49:2241–2251.

Moser D. E., Cupelli C. L., Barker I. R., Flowers R. M., Bowman J. R., Wooden J., and Hart J. R. 2011. New zircon shock phenomena and their use for dating and reconstruction of large impact structures revealed by electron nanobeam (EBSD, CL, EDS) and isotopic U-Pb and (U-Th)/He analysis of the Vredefort dome. *Canadian Journal of Earth Sciences* 48:117–139.

Moser D. E., Chamberlain K. R., Tait K. T., Schmitt A. K., Darling J. R., Barker I. R., and Hyde B. C. 2013. Solving the Martian meteorite age conundrum using micro-baddeleyite and launch-generated zircon. *Nature* 499:454–457.

Papapavlou K., Darling J. R., Moser D. E., Barker I. R., White L. F., Lightfoot P. C., Storey C. D., and Dunlop J.

2018. U-Pb isotopic dating of titanite microstructures: Potential implications for the chronology and identification of large impact structures. *Contributions to Mineralogy and Petrology* 173:1–15.

Pernet-Fisher J. F., Joy K. H., Martin D. J. P., and Donaldson Hanna K. L. 2017. Assessing the shock state of the lunar highlands: Implications for the petrogenesis and chronology of crustal anorthosites. *Scientific Reports* 7:5888.

Pickersgill A. E., Flemming R. L., and Osinski G. R. 2015. Toward quantification of strain-related mosaicity in shocked lunar and terrestrial plagioclase by in situ micro-X-ray diffraction. *Meteoritics & Planetary Science* 50:1851–1862.

Premo W. R. and Tatsumoto M. 1992. U-Th-Pb, Rb-Sr, and Sm-Nd isotopic systematics of lunar troctolite cumulate 76535: Implications on the age and origin of this early lunar, deep-seated cumulate. Proceedings, 22nd Lunar and Planetary Science Conference. pp. 381–397.

Reed S. J. B. 2005. *Electron microprobe analysis and scanning electron microscopy in geology*. Cambridge, UK: Cambridge University Press. p. 189.

Rubin A. E. 2015. Maskelynite in asteroidal, lunar and planetary basaltic meteorites: An indicator of shock pressure during impact ejection from their parent bodies. *Icarus* 257:221–229.

Rubin A. E., Scott E. R. D., and Keil K. 1997. Shock metamorphism of enstatite chondrites. *Geochimica et Cosmochimica Acta* 61:847–858.

Russell S. S., Joy K. H., Jeffries T. E., Consolmagno G. J., and Kearsley A. 2014. Heterogeneity in lunar anorthosite meteorites: Implications for the lunar magma ocean model. *Philosophical Transactions. Series A, Mathematical, Physical, and Engineering Sciences* 372:20130241.

Ryder G., Stoeser D. B., Marvin U. B., Bower J. F., and Wood J. A. 1975. Boulder 1, Station 2, Apollo 17: Petrology and petrogenesis. *The Moon* 14:327–357.

Saal A. E., Hauri E. H., Cascio M. L., Van Orman J. A., Rutherford M. C., and Cooper R. F. 2008. Volatile content of lunar volcanic glasses and the presence of water in the Moon's interior. *Nature* 454:192–195.

Sarafian A. R., Roden M. F., and Patiño-Douce A. E. 2013. The volatile content of vesta: Clues from apatite in eucrites. *Meteoritics & Planetary Science* 48:2135–2154.

Sclar C. B. and Bauer J. F. 1975. Shock-induced subsolidus reduction-decomposition of orthopyroxene and shock induced melting of norite 78235. Proceedings, 6th Lunar Science Conference. pp. 799–820.

Sclar C. B. and Bauer J. F. 1976. Subsolidus reduction phenomena in lunar norite 78235: Observations and interpretations. Proceedings, 7th Lunar Science Conference. pp. 2493–2508.

Sclar C. B. and Morzenti S. P. 1972. Electron microscopy of some experimentally shocked counterparts of lunar minerals. Proceedings, 3rd Lunar Science Conference. pp. 1121–1132.

Sippel R. F. and Spencer A. B. 1970. Cathodoluminescence properties of lunar rocks. *Science* 167:677–679.

Snape J. F., Nemchin A. A., Grange M. L., Bellucci J. J., Thiessen F., and Whitehouse M. J. 2016. Phosphate ages in Apollo 14 breccias: Resolving multiple impact events with high precision U-Pb SIMS analyses. *Geochimica et Cosmochimica Acta* 174:13–29.

Steele I. M. 1975. Mineralogy of lunar norite 78235: Second lunar occurrence of P21ca pyroxenes from Apollo 17 soils. *American Mineralogist* 60:1086–1091.

Stoeser D. B., Marvin U. B., Wood J. A., Wolfe R. W., and Bower J. F. 1974. Petrology of a stratified boulder from South Massif, Taurus-Littrow. Proceedings, 5th Lunar Science Conference. pp. 355–377.

Stöffler D. 1971. Progressive metamorphism and classification of shocked and brecciated crystalline rocks at impact craters. *Journal of Geophysical Research* 76:5541–5551.

Stöffler D. and Langenhorst F. 1994. Shock metamorphism of quartz in nature and experiment: I. Basic observation and theory. *Meteoritics & Planetary Science* 29:155–181.

Stöffler D., Ostertag R., Jammes C., Pfannschmidt G., Gupta P. R. S., Simon S. B., Papike J. J., and Beauchamp R. H. 1986. Shock metamorphism and petrography of the Shergotty achondrite. *Geochimica et Cosmochimica Acta* 50:889–903.

Stöffler D., Keil K., and Edward R. D. S. 1991. Shock metamorphism of ordinary chondrites. *Geochimica et Cosmochimica Acta* 55:3845–3867.

Tartèse R. and Anand M. 2013. Late delivery of chondritic hydrogen into the lunar mantle: Insights from mare basalts. *Earth and Planetary Science Letters* 361:480–486.

Tartèse R., Anand M., Barnes J. J., Starkey N. A., Franchi I. A., and Sano Y. 2013. The abundance, distribution, and isotopic composition of hydrogen in the Moon as revealed by basaltic lunar samples: Implications for the volatile inventory of the Moon. *Geochimica et Cosmochimica Acta* 122:58–74.

Tartèse R., Anand M., McCubbin F. M., Elardo S. M., Shearer C. K., and Franchi I. A. 2014. Apatites in lunar KREEP basalts: The missing link to understanding the H isotope systematics of the Moon. *Geology* 42:363–366.

Terada K., Saiki T., Oka Y., Hayasaka Y., and Sano Y. 2005. Ion microprobe U-Pb dating of phosphates in lunar basaltic breccia, Elephant Moraine 87521. *Geophysical Research Letters* 32:L20202.

Terada K., Sasaki Y., Anand M., Joy K. H., and Sano Y. 2007. Uranium–lead systematics of phosphates in lunar basaltic regolith breccia, Meteorite Hills 01210. *Earth and Planetary Science Letters* 259:77–84.

Thiessen F., Nemchin A. A., Snape J. F., Whitehouse M. J., and Bellucci J. J. 2017. Impact history of the Apollo 17 landing site revealed by U-Pb SIMS ages. *Meteoritics & Planetary Science* 52:584–611.

Walton E. L., Sharp T. G., Hu J., and Filiberto J. 2014. Heterogeneous mineral assemblages in Martian meteorite Tissint as a result of a recent small impact event on Mars. *Geochimica et Cosmochimica Acta* 140:334–348.

Walton C., Cernok A., and Anand M. 2018. The formation and shock-history of phosphate minerals in Chelyabinsk (LL5). LPI Contribution 2067. Moscow, Russia: 81st Annual Meeting of The Meteoritical Society, July 22–27, 2018.

Warren P. H. 1993. A consise compilation of petrologic information on possibly pristine nonmare Moon rocks. *American Mineralogist* 78:360–376.

Webster J. D. and Piccoli P. M. 2015. Magmatic apatite: A powerful, yet deceptive, mineral. *Elements* 11:177–182.

White L. F., Darling J. R., Moser D. E., Reinhard D. A., Prosa T. J., Bullen D., Olson D., Larson D. J., Lawrence D., and Martin I. 2017. Atomic-scale age resolution of planetary events. *Nature Communications* 8:15597.

White L. F., Darling J. R., Moser D. E., Reinhard D. A., Dunlop J., Larson D. J., Lawrence D., and Martin I. 2018a. Complex nanostructures in shocked, annealed, and

metamorphosed baddeleyite defined by atom probe tomography. In *Microstructural geochronology*, edited by Moser D. E., Corfu F., Darling J. R., Reddy S. M., and Tait K. Hoboken, New Jersey: John Wiley & Sons, Inc. pp. 351–367.

White L. F., Darling J. R., Moser D. E., Cayron C., Barker I., Dunlop J., and Tait K. T. 2018b. Baddeleyite as a widespread and sensitive indicator of meteorite bombardment in planetary crusts. *Geology* 46:719–722.

Wilson R. M., Elliott J. C., and Dowker S. E. P. 1999. Rietveld refinement of the crystallographic structure of human dental enamel apatites. *American Mineralogist* 84 (9):1406–1414.

Winzer S. R. 1975. Origin of 78235, a lunar norite cumulate. Proceedings, 6th Lunar Science Conference. pp. 1219–1229.

Xie X., Minitti M. E., Chen M., Okwang M. H., Wang D., Shu J., and Fei Y. 2002. Natural high-pressure polymorph of merrillite in the shock veins of the Suizhou meteorite. *Geochimica et Cosmochimica Acta* 66:2439–2444.

Xie X., Minitti M. E., Chen M., Mao H.-K., Wang D., Shu J., and Fei Y. 2003. Tuite, γ-Ca3(PO4)2: A new mineral from the Suizhou L6 chondrite. *European Journal of Mineralogy* 15:1001–1005.

Xie X., Zhai S., Chen M., and Yang H. 2013. Tuite, γ-Ca3 (PO4)2, formed by chlorapatite decomposition in a shock vein of the Suizhou L6 chondrite. *Meteoritics & Planetary Science* 48:1515–1523.

Xie X., Yang H., Gu X., and Downs R. T. 2015. Chemical composition and crystal structure of merrillite from the Suizhou meteorite. *American Mineralogist* 100:2753–2756.

Xie S., Shieh R., and Osinski G. R. 2017. Raman study of shock effects in Lunar anorthite from the Apollo Missions (abstract #1596). 48th Lunar and Planetary Science Conference. CD-ROM.

Zhai S. and Wu X. 2010. X-ray diffraction study of β-Ca3 (PO4)2 at high pressure. *Solid State Communications* 150:443–445.

SUPPORTING INFORMATION

Additional supporting information may be found online in the Supporting Information section at the end of the article.

Fig. S1. Plane polarized, crossed-polarized, and CL image of studied minerals.

Fig. S2. Inverse pole figures (IPF) and corresponding pole figures of all apatites and merrillites from S1 to S5, presented in the main text (Figs. 3 and 4).

Fig. S3. Other examples of highly (S5) shocked apatite and merrillite from sample 78235,43.

Fig. S4. CL image of apatite and merrillite.

Fig. S5. Recrystallized merrillite and plagioclase.

Table S1. Overview of electron backscatter diffraction (EBSD) instrument and analytical conditions.

Table S2. Peak fitting parameters in Raman spectra of plagioclase, apatite, and merrillite.

Data S1. Raman spectra of plagioclase, apatite and merrillite presented in Fig. 2.